

Density functional theory of gas-liquid phase separation in dilute binary mixtures

Ryuichi Okamoto¹ and Akira Onuki²

¹*Department of Chemistry, Tokyo Metropolitan University, Hachioji, Tokyo 192-0397, Japan*

²*Department of Physics, Kyoto University, Kyoto 606-8502, Japan*

(Dated: December 31, 2015)

We examine statics and dynamics of phase-separated states of dilute binary mixtures using density functional theory. In our systems, the difference in the solvation chemical potential $\Delta\mu_s$ between liquid and gas is considerably larger than the thermal energy $k_B T$ for each solute particle and the attractive interaction among the solute particles is weaker than that among the solvent particles. In these conditions, the saturated vapor pressure increases by an amount equal to the solute density in liquid multiplied by the large factor $k_B T \exp(\Delta\mu_s/k_B T)$. As a result, phase separation is induced at low solute densities in liquid and the new phase remains in gaseous states, while the liquid pressure is outside the coexistence curve of the solvent. This explains the widely observed formation of stable nanobubbles in ambient water with a dissolved gas. We calculate the density and stress profiles across planar and spherical interfaces, where the surface tension decreases with increasing the interfacial solute adsorption. We realize stable solute-rich bubbles with radius about 30 nm, which minimize the free energy functional. We then study dynamics around such a bubble after a decompression of the surrounding liquid, where the bubble undergoes a damped oscillation. In addition, we present some exact and approximate expressions for the surface tension and the interfacial stress tensor.

I. INTRODUCTION

Much attention has been paid to complex interactions among dissolved particles and solvent molecules [1–3]. In liquid water, hydrophobic particles deform the surrounding hydrogen bond structure [4–6], resulting in a solvation chemical potential μ_s much larger than the thermal energy $k_B T$ (per particle). As a result, they tend to aggregate in liquid water at ambient conditions (room temperature and 1 atm pressure). In simulations of a hard-sphere particle with radius a in ambient water, μ_s is of order $4\pi a^2 \sigma$ for $a > 1$ nm, where σ is the gas-liquid surface tension [4–6]. Such large particles are thus strongly hydrophobic ($\mu_s \sim 180 k_B T$ for $a \sim 1$ nm). Another notable example is the solvent-mediated interaction among colloidal particles in near-critical mixture solvents [7–14], where one fluid component is preferentially adsorbed on the colloidal surfaces, largely deforming the surrounding critical fluctuations and often leading to local phase separation (bridging).

Recently, we have presented a theory on the formation of small bubbles in ambient water containing a small amount of a dissolved gas [15]. As a typical example, O_2 is *mildly hydrophobic* with $\mu_s = 3.44 k_B T$ in liquid water at $T = 300$ K. As a unique feature of ambient liquid water, it has pressures only slightly higher than the saturated vapor pressure or is immediately outside the coexistence curve (CX) in the phase diagram. Moreover, the van der Waals interaction among O_2 molecules is relatively weak as compared to the hydrogen bond interaction. In fact, the critical temperature of water is considerably higher than that of O_2 (647.3 K for water and 154.6 K for O_2). In this situation, O_2 molecules tend to be expelled from liquid water in the form of oxygen-rich bubbles (or films) above a very low threshold concentration outside CX. In many experiments, small bubbles, often called nanobubbles, have been observed in the

bulk and on hydrophobic walls in ambient water [16, 17]. Their radius is typically of order 10 – 100 nm and their life time is very long. In our theory [15], they are thermodynamically stable, minimizing the free energy including the surface tension. As a similar phenomenon, long-lived heterogeneities have been observed in one-phase states of aqueous mixtures with addition of a small amount of a salt or a hydrophobic solute [18–20]. These phenomena emerge as examples of selective solvation effects [18].

In this paper, we investigate two-phase states of dilute binary mixtures at $T = 300$ K using the density functional theory (DFT) [3, 21–24] on the basis of the Carnahan-Starling model for binary mixtures [25, 26]. As in the case of O_2 in water, we determine the model parameters in Ref. [26] such that μ_s is $3.44 k_B T$ in liquid and the solute-solute attractive interaction is weaker than that among the solvent particles. In these conditions, we consider gas-liquid coexistence separated by planar and spherical interfaces, where we calculate the density and stress profiles and the solute-induced deviations of thermodynamic quantities. For our parameter values, there also arises a significant interfacial adsorption of the solute, which leads to a reduction of the surface tension σ in accord with the Gibbs law [27]. We are interested in stable solute-induced bubbles minimizing the free energy functional of DFT. The radius of a stable bubble R_m is larger than the critical radius of nucleation R_c [28–31], but remains to be very small.

Within the scheme of DFT, some attempts have been made to describe dynamics of colloidal particles in solvent without [32, 33] and with [24, 34–36] the hydrodynamic interaction. We also mention dynamic van der Waals theory with gradient entropy and energy [37], which is a generalization of the original van der Waals theory [38]. Using this scheme, Teshigawara and one of the present authors (A.O.) numerically studied evaporation and condensation in inhomogeneous temperature [39–41]. In their

simulations, Tanaka and Araki treated colloidal particles as highly viscous droplets with diffuse interfaces [11]. Their method has been used to study hydrodynamics and phase separation around colloidal particles [11–14]. In this paper, we present dynamic equations for binary mixtures composed of small particles, where DFT and hydrodynamics are incorporated on acoustic and diffusive timescales. As an application, we study dynamics around a bubble after a decompression of the surrounding liquid.

Bubble dynamics is very complicated, where hydrodynamics and gas-liquid phase transition are inseparably coupled [42–45]. On short timescales, the pressure balance does not hold at the interface and the bubble motions become oscillatory accompanied by acoustic disturbances. In particular, they have been studied extensively under applied acoustic field. On long timescales, the bubble growth is governed by the thermal diffusion in one-component fluids [30, 31] and by the slower solute diffusion in mixtures [15, 43]. In this paper, we aim to study these characteristic features.

This paper is organized as follows. In Sec.II, we will present the background of DFT related to our problem. In Sec.III, we will examine two-phase states of dilute binary mixtures including a considerably large solvation chemical potential in DFT. In Sec.IV, dynamics around a bubble will be studied numerically. In Appendix B, we will present some relations for the interfacial stress tensor in the exact statistical theory.

II. THEORETICAL BACKGROUND

A. Free energy functional

We treat a neutral binary mixture in DFT [21–24], where the first species is a solvent and the second one is a dilute solute. The number densities $n_1(\mathbf{r})$ and $n_2(\mathbf{r})$ are coarse-grained smooth functions of space. There are no Coulombic and dipolar interactions. Hereafter, the temperature T is assumed to be a homogeneous constant ($= 300$ K) and the Boltzmann constant is set equal to 1.

In DFT, the Helmholtz free energy functional consists of two parts as $\mathcal{F} = \mathcal{F}_h + \mathcal{F}_a$. The first part is of the local form $\mathcal{F}_h = \int d\mathbf{r} f(n_1, n_2)$ with the free energy density,

$$f = T \sum_i n_i [\ln(n_i \lambda_i^3) - 1] + f_h(n_1, n_2) + \sum_i n_i U_i, \quad (1)$$

where $\lambda_i (\propto T^{-1/2})$ is the thermal de Broglie length and the space integral is within the cell. The $f_h(n_1, n_2)$ arises from the short-ranged repulsive interaction and is taken to assume the binary Carnahan-Starling form[26]. See Appendix A for its details. The $U_i(\mathbf{r})$ is the externally applied potential such as the wall or gravitational potential. The second part \mathcal{F}_a arises from the attractive

interaction and is of the form,

$$\mathcal{F}_a = \frac{1}{2} \int d\mathbf{r}_1 \int d\mathbf{r}_2 \sum_{i,j} \phi_{ij}(r_{12}) n_i(\mathbf{r}_1) n_j(\mathbf{r}_2). \quad (2)$$

Here, $\phi_{ij}(r_{12})$ is an effective potential, which is negative and continuously depends on the distance $r_{12} = |\mathbf{r}_1 - \mathbf{r}_2|$. Its space integral should be finite, so we introduce

$$w_{ij} = -4\pi \int_0^\infty dr r^2 \phi_{ij}(r). \quad (3)$$

We define the chemical potentials of the two species as the functional derivatives $\mu_i(\mathbf{r}) = \delta\mathcal{F}/\delta n_i(\mathbf{r})$. For the present model they are expressed as

$$\mu_i = T \ln(n_i \lambda_i^3) + \mu_{hi} + \mu_{ai} + U_i, \quad (4)$$

where $\mu_{hi} = \partial f_h / \partial n_i$ is the repulsive part and μ_{ai} is the attractive part expressed in the convolution form as

$$\mu_{ai} = \int d\mathbf{r}_1 \sum_j \phi_{ij}(r_1) n_j(\mathbf{r} - \mathbf{r}_1). \quad (5)$$

For homogeneous n_j we have $\mu_{ai} = -\sum_j w_{ij} n_j$.

If variations of n_i are sufficiently slow, we can use the gradient expansion of \mathcal{F}_a [22, 31, 46] to obtain $\mathcal{F}_a \cong \int d\mathbf{r} \sum_{ij} [-w_{ij} n_i n_j / 2 + C_{ij} \nabla n_i \cdot \nabla n_j / 2]$, where

$$C_{ij} = -\frac{2\pi}{3} \int_0^\infty dr r^4 \phi_{ij}(r). \quad (6)$$

With this approximation, we recognize the relationship between DFT and the original van der Waals theory with the gradient free energy[38].

In the literature[22–24], $\phi_{ij}(r)$ has often been set equal to the attractive part of the Lennard-Jones potential characterized by the parameters d_{ij} and ϵ_{ij} . For $r > 2^{1/6} d_{ij}$ it is expressed as

$$\phi_{ij}(r) = 4\epsilon_{ij} [(d_{ij}/r)^{12} - (d_{ij}/r)^6], \quad (7)$$

For $r \leq 2^{1/6} d_{ij}$, we define $\phi_{ij}(r) = -\epsilon_{ij}$. In our numerical analysis, at $T = 300$ K, we set

$$\begin{aligned} d_1 &= d_{11} = 3.0 \text{ \AA}, \quad d_2 = d_{22} = 2.48 \text{ \AA}, \quad d_{12} = 2.74 \text{ \AA}, \\ \epsilon_{11} &= 588.76 \text{ K}, \quad \epsilon_{22} = 108.53 \text{ K}, \quad \epsilon_{12} = 251.26 \text{ K}. \end{aligned} \quad (8)$$

Hereafter, we write $d_1 = d_{11}$ and $d_2 = d_{22}$ for simplicity. From Eq.(3) these values lead to $w_{11}/d_1^3 T = 30.80$, $w_{22}/d_1^3 T = 3.21$, and $w_{12}/d_1^3 T = 10.02$. Here, $\epsilon_{22}/\epsilon_{11} = 0.18$, so the solute-solute attractive interaction is much weaker than the solvent-solvent one. This is one of the conditions of the solute-induced bubble formation[15]. In two-phase coexistence of the first species, the liquid and gas densities are calculated as $n_\ell = 1.0 d_1^{-3} = 37 \text{ nm}^{-3}$ and $n_g = 2.05 \times 10^{-5} d_1^{-3} = 7.7 \times 10^{-4} \text{ nm}^{-3}$. On the other hand, in real ambient water, they are known to be $n_\ell \sim 33 \text{ nm}^{-3}$ and $n_g \sim 10^{-3} \text{ nm}^{-3}$.

B. Stress tensor in DFT

We examine the stress tensor $\Pi_{\alpha\beta}(\mathbf{r})$ ($\alpha, \beta = x, y, z$) in DFT. If f_h is of the local form, the repulsive part of $\Pi_{\alpha\beta}$ is diagonal as $p_h\delta_{\alpha\beta}$ with

$$p_h = n_1\mu_{h1} + n_2\mu_{h2} - f_h. \quad (9)$$

However, the attractive pair interaction gives rise to off-diagonal components. We express $\Pi_{\alpha\beta}$ as

$$\begin{aligned} \Pi_{\alpha\beta} = & (Tn + p_h)\delta_{\alpha\beta} - \int d\mathbf{r}_1 \int d\mathbf{r}_2 \sum_{ij} \frac{x_{12\alpha}x_{12\beta}}{2r_{12}} \\ & \times \phi'_{ij}(r_{12})\delta_s(\mathbf{r}, \mathbf{r}_1, \mathbf{r}_2)n_i(\mathbf{r}_1)n_j(\mathbf{r}_2), \end{aligned} \quad (10)$$

where $n = n_1 + n_2$, $\phi'_{ij} = d\phi_{ij}/dr$, and $x_{12\alpha} = x_{1\alpha} - x_{2\alpha}$. We use the Irving-Kirkwood δ function[31, 47–49],

$$\delta_s(\mathbf{r}, \mathbf{r}_1, \mathbf{r}_2) = \int_0^1 d\lambda \delta(\mathbf{r} - \lambda\mathbf{r}_1 - (1-\lambda)\mathbf{r}_2), \quad (11)$$

which is nonvanishing only when \mathbf{r} is on the line segment connecting \mathbf{r}_1 and \mathbf{r}_2 . The integrand is appreciable only if $|\mathbf{r} - \mathbf{r}_1|$ and $|\mathbf{r} - \mathbf{r}_2|$ are shorter than the potential range. The expression (10) is approximate, while the exact one in terms of δ_s [47] will be given in Appendix B.

Using $\mathbf{r}_{12} \cdot \nabla \delta_s(\mathbf{r}, \mathbf{r}_1, \mathbf{r}_2) = \delta(\mathbf{r} - \mathbf{r}_2) - \delta(\mathbf{r} - \mathbf{r}_1)$ and $\phi'_{ij}(r_{12})x_{12\alpha}/r_{12} = \partial\phi_{ij}(r_{12})/\partial x_{1\alpha}$, we find

$$\sum_{\beta} \nabla_{\beta} \Pi_{\alpha\beta} = \sum_i n_i \nabla_{\alpha} (\mu_i - U_i), \quad (12)$$

where $\nabla_{\beta} = \partial/\partial x_{\beta}$. This relation holds generally for homogeneous T (even in nonequilibrium). In equilibrium, μ_1 and μ_2 are homogeneous, which leads to the mechanical equilibrium condition $\sum_{\beta} \nabla_{\beta} \Pi_{\alpha\beta} + \sum_i n_i \nabla_{\alpha} U_i = 0$ from Eq.(12). For homogeneous n_i , we have the diagonal form $\Pi_{\alpha\beta} = (Tn + p_h - \sum_{ij} w_{ij}n_i n_j/2)\delta_{\alpha\beta}$ as in the van der Waals theory[31, 38].

C. Equilibrium in one-dimensional geometry

We assume that our fluid is between parallel walls separated by L . The wall area much exceeds L^2 . The U_i in Eq.(1) is the wall potential. Then, all the physical quantities depend only on z . We do not consider capillary wave fluctuations, which are inhomogeneous in the xy plane on large scales. They are known to give rise to broadening of the profile [22, 50, 51].

1. Pressure balance and grand potential

In equilibrium, the chemical potentials in Eq.(4) are homogeneous in the cell as $\mu_1 = \mu_1^0$ and $\mu_2 = \mu_2^0$, where

μ_1^0 and μ_2^0 are constants. After integration in the xy plane, the attractive part μ_{ai} in Eq.(5) becomes

$$\mu_{ai}(z) = 2\pi \sum_j \int dz_1 \Phi_{ij}(z - z_1)n_j(z_1), \quad (13)$$

where we define the function,

$$\Phi_{ij}(z) = \int_{|z|}^{\infty} dr r \phi_{ij}(r). \quad (14)$$

Here, $\int dz \Phi_{ij}(z) = 2 \int_0^{\infty} dr r^2 \phi_{ij}(r) = -w_{ij}/2\pi$, so we have $\mu_{ai} = -\sum_j w_{ij}n_j$ for homogeneous n_j .

From Eq.(12) the stress balance along the z axis gives

$$\frac{d}{dz} \Pi_{zz} = -\sum_i n_i U'_i, \quad (15)$$

where $U'_i = dU_i/dz$ and Π_{zz} consists of three parts as

$$\Pi_{zz}(z) = Tn(z) + p_h(z) + p_a(z). \quad (16)$$

From Eq.(10) the attractive part p_a is expressed as

$$p_a = 2\pi \int_z^L dz_1 \int_0^z dz_2 \sum_{ij} z_{12} \phi_{ij}(z_{12})n_i(z_1)n_j(z_2), \quad (17)$$

where $z_{12} = z_1 - z_2$ and $z_2 < z < z_1$ in the integrand. Here, use has been made of the relation,

$$\int d\mathbf{r}_{1\perp} \delta_s(\mathbf{r}, \mathbf{r}_1, \mathbf{r}_2) = [\theta(z - z_2) - \theta(z - z_1)]/z_{12}, \quad (18)$$

where $d\mathbf{r}_{1\perp} = dx_1 dy_1$ and $\theta(u)$ is the step function (equal to 1 for $u > 0$ and to 0 for $u \leq 0$). From Eq.(15), Π_{zz} is homogeneous far from the walls and its value is written as p_b^0 . This means that if two phases are separated by a planar interface far from the walls, the pressures in the bulk two regions are commonly given by p_b^0 .

The grand potential $\Omega = \int d\mathbf{r} \omega$ is the space integral of its density ω . In the present 1D case, we find

$$\begin{aligned} \omega &= f + \frac{1}{2} \sum_i \mu_{ai} n_i - \sum_i \mu_i n_i \\ &= -\Pi_{zz} + p_a - \frac{1}{2} \sum_i \mu_{ai} n_i. \end{aligned} \quad (19)$$

In the second line, use has been made of Eqs.(13), (16), and (17). In the bulk, both p_a and $\sum_{ij} n_i \mu_{ai}/2$ tend to $-\sum_{ij} w_{ij}n_i n_j/2$. Hence, ω deviates from its bulk value $-p_b^0$ only near the interface or the walls.

2. Surface tension

Let a planar interface parallel to the xy plane separate gas and liquid phases far from the walls, where $U_i = 0$ and $\Pi_{zz} = p_{\text{ex}} = \text{const.}$ around the interface, where p_{ex} is

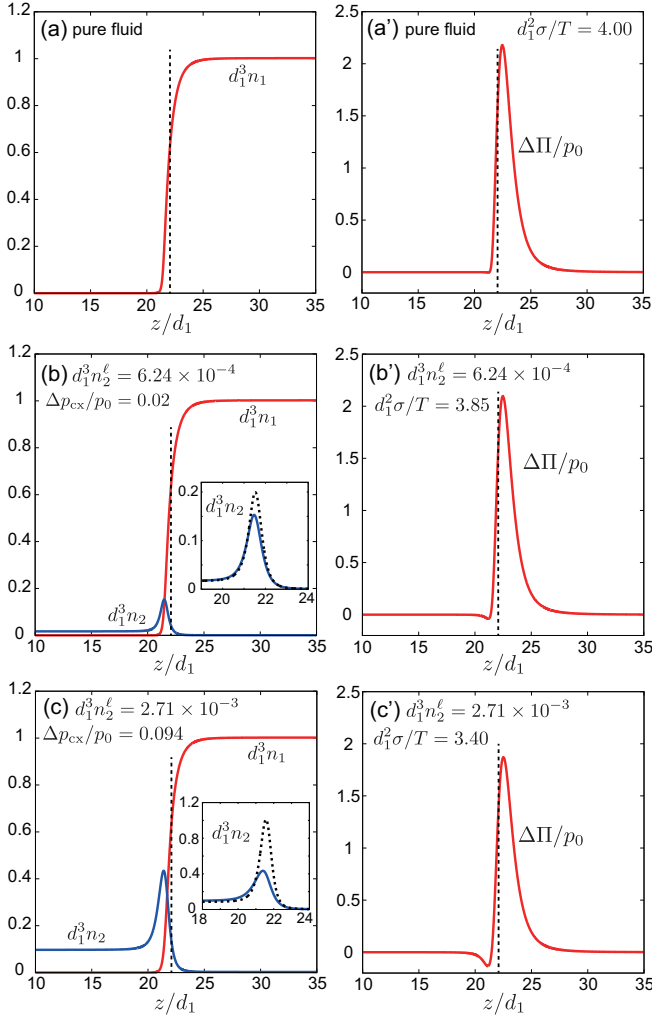


FIG. 1: Left: Densities $n_1(z)$ and $n_2(z)$ vs z/d_1 around planar interfaces at $T = 300$ K far below the criticality. Solvent and solute densities ($n_1^\ell, n_2^\ell, n_1^g, n_2^g$) in bulk liquid and gas are (a) $(1.0, 0, 2.05 \times 10^{-5}, 0)$ (without solute), (b) $(1.0, 6.24 \times 10^{-4}, 2.40 \times 10^{-5}, 2.02 \times 10^{-2})$, and (c) $(1.0, 2.71 \times 10^{-3}, 4.28 \times 10^{-5}, 0.097)$ in units of d_1^{-3} . In (b) and (c) (inset), numerical $n_2(z)$ (bold line) is compared with low density expression in Eq.(37) (dotted line) around the adsorption peak. Right: Stress difference $\Delta\Pi(z) = \Pi_{zz}(z) - \Pi_{xx}(z)$ divided by $p_0 = Td_1^{-3} = 153$ MPa vs z/d_1 , calculated from Eqs.(27) and (28) for (a), (b), and (c). Its integral is the surface tension σ , which is (a) $4.00 (= \sigma_0)$, (b) 3.85 , and (c) 3.40 in units of Td_1^{-2} . The coexisting pressure p_{cx} is (a) $2.1 \times 10^{-5} (= p_{cx}^0)$, (b) 2.0×10^{-2} , and (c) 0.094 in units of Td_1^{-3} . Vertical broken lines indicate the position of the Gibbs dividing surface in Eq.(20).

the coexisting (saturated pressure) of the mixture. The left panels of Fig.1 display equilibrium density profiles $n_1(z)$ and $n_2(z)$, which are calculated from the method in Appendix C. They tend to n_1^ℓ and n_2^ℓ in liquid ($z - z_{\text{int}} \gg d_1$) and n_1^g and n_2^g in gas ($z_{\text{int}} - z \gg d_1$), respectively. We

can determine the interface position z_{int} by

$$z_{\text{int}} = \int_0^L dz [n_1(z) - n_1^g] / [n_1^\ell - n_1^g], \quad (20)$$

using the solvent density profile $n_1(z)$ [27]. Note that n_1^ℓ is nearly fixed at $1.0d_1^{-3}$ because the liquid compressibility is small.

From Eq.(19), the surface tension σ is the z -integral of $p_a - \sum_i n_i \mu_{ai} / 2$. Thus, Eqs.(13) and (17) gives

$$\sigma = \frac{1}{2} \int dz_1 \int dz_2 \sum_{ij} \Theta_{ij}(z_{12}) n_i(z_1) n_j(z_2), \quad (21)$$

where we define the function,

$$\Theta_{ij}(z) = 2\pi [z^2 \phi_{ij}(|z|) - \Phi_{ij}(z)]. \quad (22)$$

Here, from $\int dz \Theta_{ij}(z) = 0$, we can replace $n_i(z_1) n_j(z_2)$ by $[n_i(z_1) - n_i(z_2)][n_j(z_2) - n_j(z_1)] / 2$ in Eq.(21); then, the integrand is nonvanishing only near the interface. See Appendix B for the exact formula for σ [48].

Furthermore, we introduce another function $K_{ij}(z)$ by

$$K_{ij}(z) = \frac{\pi}{2} \int_{|z|}^{\infty} dr r (z^2 - r^2) \phi_{ij}(r). \quad (23)$$

This function is related to Φ_{ij} and Θ_{ij} as

$$\frac{d}{dz} K_{ij}(z) = \pi z \Phi_{ij}(z), \quad \frac{d^2}{dz^2} K_{ij}(z) = -\frac{1}{2} \Theta_{ij}(z). \quad (24)$$

In terms of K_{ij} and $n'_i = dn_i/dz$, σ is expressed as

$$\sigma = \int dz_1 \int dz_2 \sum_{ij} K_{ij}(z_{12}) n'_i(z_1) n'_j(z_2). \quad (25)$$

This leads to the well-known form $\sigma = \int dz \sum_{ij} C_{ij} n'_i n'_j$ in the gradient theory [22, 31, 46], where $\int dz K_{ij}(z) = C_{ij}$ from Eqs.(6) and (23). If we assume the Lennard-Jones form in Eq.(7), we have $K_{ij}(z) \sim |z|^{-2}$, $\Phi_{ij}(z) \sim |z|^{-4}$, and $\Theta_{ij}(z) \sim |z|^{-4}$ for large $|z| \gg d_1$.

The surface tension σ of neutral fluids can generally be expressed by the Bakker formula[22, 48, 52, 53],

$$\sigma = \int dz [\Pi_{zz}(z) - \Pi_{xx}(z)] = \int dz \Delta\Pi(z). \quad (26)$$

The stress difference $\Delta\Pi(z) \equiv \Pi_{zz}(z) - \Pi_{xx}(z)$ is nonvanishing only near the interface. In DFT, we start with Eq.(10) and use Eq.(18) to obtain

$$\Delta\Pi(z) = \int_z^L dz_1 \int_0^z dz_2 \sum_{ij} \frac{\Theta_{ij}(z_{12})}{z_{12}} n_i(z_1) n_j(z_2), \quad (27)$$

where $z_1 > z > z_2$ in the integrand. With respect to z , integration of $\Delta\Pi(z)$ in Eq.(27) gives Eq.(21), while its derivative is written in the single integral form,

$$\frac{d\Delta\Pi}{dz} = \int_0^\infty d\xi \sum_{ij} \frac{\Theta_{ij}(\xi)}{\xi} [n_i(z+\xi) - n_i(z-\xi)] n_j(z). \quad (28)$$

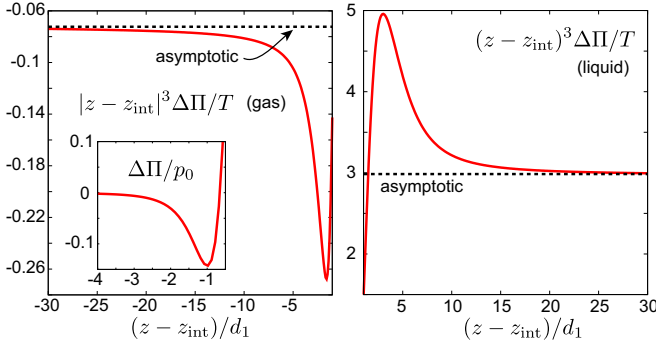


FIG. 2: $|z - z_{\text{int}}|^3 \Delta\Pi(z)/T$ vs $(z - z_{\text{int}})/d_1$ in gas (left) and liquid (right) for case (c) in Fig.1 with $n_2^\ell = 4.28 \times 10^{-5} d_1^{-3}$. It tends to -0.0721 (left) and to 3.00 (left) in agreement with Eq.(29). In the inset (left) $\Delta\Pi/p_0$ is expanded in gas, which has a small negative minimum.

Far from the interface, $\Delta\Pi(z)$ decays as $\propto |z - z_{\text{int}}|^{-3}$ if the Lennard-Jones potential in Eq.(7) is assumed. In Eq.(28), we may replace $[n_i(z + \xi) - n_i(z - \xi)]n_j(z)$ by $(n_i^\ell - n_i^g)n_j^\ell$ for $\xi > z - z_{\text{int}} \gg d_1$. Then, for $z - z_{\text{int}} \gg d_1$, we find $d\Delta\Pi(z)/dz \sim |z - z_{\text{int}}|^{-4}$ and

$$\Delta\Pi(z) \cong \frac{\pi}{2} \sum_{ij} \epsilon_{ij} d_{ij}^6 (n_i^\ell - n_i^g) n_j^\ell |z - z_{\text{int}}|^{-3}. \quad (29)$$

In the gas side with $z_{\text{int}} - z \gg d_1$, the corresponding tail is obtained if n_j^ℓ in Eq.(29) is replaced by $-n_j^g$. Thus, its amplitude becomes very small in the gas side. Remarkably, the above form of $\Delta\Pi(z)$ holds exactly for Lennard-Jones systems (see Appendix B). Note that the density profiles $n_i(z)$ themselves decay as $|z - z_{\text{int}}|^{-3}$, as will be shown in Eqs.(43)-(45) [23, 54, 55]. In contrast, in the gradient theory, we have $\Delta\Pi(z) = \sum_{ij} C_{ij} n_i'(z) n_j'(z)$ [31], which decays exponentially far from the interface.

In the right panels of Fig.1, we plot $\Delta\Pi(z)$ calculated from Eq.(28), where its integral ($= \sigma$) decreases with increasing the solute amount due to its interfacial adsorption (see Fig.5). In the liquid side, its decay is roughly exponential as $\exp[-(z - z_{\text{int}})/1.0d_1]$ for $0 < z - z_{\text{int}} \lesssim 3d_1$ and is algebraic as in Eq.(29) for larger $z - z_{\text{int}}$. However, in the gas side, it decays rapidly and its small tail is not apparent. To detect the tails unambiguously, we plot $|z - z_{\text{int}}|^3 \Delta\Pi(z)/T$ in gas and liquid in Fig.2.

3. Solid-fluid surface free energy

We also derive the expression for the solid-fluid surface free energy σ_w per unit area, which is needed in discussions of the wetting and drying transitions [21, 23, 46]. Near the wall at $z = 0$, we find $\int_0^\infty dz (\Pi_{zz} - p_b^0) = \int_0^\infty dz z \sum_i n_i U_i'$ from $d[z\Pi_{zz}]/dz = \Pi_{zz} - z \sum_i n_i U_i'$, where the upper bound is pushed to infinity. Then, σ_w

is the integral of $p_a - \sum_i (\mu_{ai}/2 + zU_i')n_i$ so that

$$\sigma_w = \frac{1}{2} \int_0^\infty dz_1 \int_0^\infty dz_2 \sum_{ij} \Theta_{ij}(z_{12}) n_i(z_1) n_j(z_2) - \int_0^\infty dz z \sum_i n_i(z) U_i'(z), \quad (30)$$

where $\Theta_{ij}(z_{12})n_i(z_1)n_j(z_2)$ in the first term can be replaced by $2K_{ij}(z_{12})n_i'(z_1)n_j'(z_2)$ as in Eq.(25).

III. DILUTE BINARY MIXTURES

A. Solvation chemical potential

Here, we introduce the solvation chemical potential for each solute particle in dilute binary mixtures. The solvation effects are of great importance for various solutes including ions in aqueous fluids [18, 57–59].

In the binary Carnahan-Starling model [26], the free energy density $f(n_1, n_2)$ in Eq.(1) can be expanded as

$$f = f_w(n_1) + Tn_2[\ln(n_2\lambda_2^3) - 1 + \nu_h(n_1)], \quad (31)$$

up to order n_2 [15, 56]. Here, $f_w(n_1) = f(n_1, 0)$ is the low density limit of the free energy density (excluding the attractive part) and $\nu_h(n_1)$ arises from the repulsive interaction between a solute particle and the surrounding solvent. The solute-solute interaction is neglected here. As will be shown in Appendix A, we express ν_h in terms of $\eta_1 = \pi d_1^3 n_1/6$ and $u_1 = \eta_1/(1 - \eta_1)$ as

$$\nu_h = (3\alpha + 6\alpha^2 - \alpha^3)u_1 + (3\alpha^2 + 4\alpha^3)u_1^2 + 2\alpha^3 u_1^3 + (3\alpha^2 - 2\alpha^3 - 1) \ln \eta_1, \quad (32)$$

where α is the solute-to-solvent size ratio,

$$\alpha = d_{22}/d_{11} = d_2/d_1. \quad (33)$$

In our numerical analysis, we set $\alpha = 0.827$ in Eq.(8).

Including the attractive interaction, the total solvation chemical potential μ_s is written as

$$\mu_s = T\nu_h + \phi_{12} * n_1. \quad (34)$$

where the second term is of the convolution from. The chemical potentials are approximately given by

$$\mu_1 = f'_w + \phi_{11} * n_1 + Tn_2\nu'_h + \phi_{12} * n_2 + U_1, \quad (35)$$

$$\mu_2 = T \ln(n_2\lambda_2^3) + \mu_s + U_2, \quad (36)$$

where $f'_w = \partial f_w / \partial n_1$ and $\nu'_h = \partial \nu_h / \partial n_1$. We have neglected terms of order n_2^2 in Eq.(35) and those of order n_2 in Eq.(36). Thus, in equilibrium, n_2 is written as

$$n_2(z) \cong n_{20} \exp[-\nu_h - \phi_{12} * n_1/T - U_2/T], \quad (37)$$

where $n_{20} = \exp(\mu_2/T)\lambda_2^{-3}$. In the insets in Fig.1, this expression and the numerically calculated $n_2(z)$ are compared. The former noticeably overestimates the adsorption peak in (c), where n_2 is not small at the peak and the repulsive solute-solute interaction is appreciable.

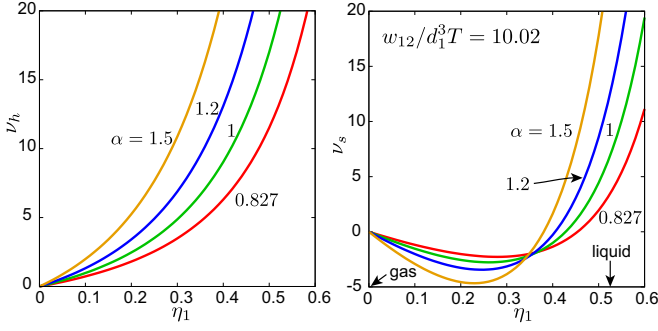


FIG. 3: (a) ν_h in Eq.(32) vs solvent volume fraction $\eta_1 = \pi d_1^3 n_1/6$ for four values of size ratio α , which is the contribution from repulsive interaction to the solvation chemical potential divided by T . Numerical analysis in this paper is performed for $\alpha = 0.827$ (lowest curve). (b) Solvation chemical potential $\nu_s = \nu_h - w_{12}n_1/T$ divided by T vs η_1 including attractive interaction in bulk with $w_{12}/d_1^3 T = 10.02$. Marked by arrows indicate values of η_1 in two phase coexistence without solute, where $\nu_s = 3.44$ at this liquid point for $\alpha = 0.827$.

We use the symbol $\nu_s(n_1)$ as the solvation chemical potential divided by T in the bulk region:

$$\nu_s(n_1) = \mu_s/T = \nu_h(n_1) - w_{12}n_1/T. \quad (38)$$

whose derivative with respect to n_1 is written as

$$\nu'_s(n_1) = \nu'_h(n_1) - w_{12}/T. \quad (39)$$

The pressure p in the bulk region satisfies the thermodynamic relation $p = \sum_i n_i \mu_i - f - \sum w_{ij} n_i n_j/2$ as in the van der Waals theory. Up to order n_2 it is written as

$$p = p_w(n_1) + T[1 + n_1 \nu'_s(n_1)]n_2, \quad (40)$$

where $p_w(n_1)$ is the pressure without solute.

In Fig.3, we plot ν_h and ν_s vs $\eta_1 = \pi d_1^3 n_1/6$ for four values of α . We recognize that ν_h increases strongly with increasing η_1 and α . In contrast, ν_s in Eq.(38) exhibits a minimum at a density between the gas and liquid densities in the pure fluid limit, n_g and n_ℓ . Such a minimum leads to solute adsorption in the gas side of the interface region (see $n_2(z)$ in Fig.1). We set $w_{12} = 10.02T d_1^3$ such that $\nu_s(n_\ell) - \nu_s(n_g) \cong \nu_s(n_\ell)$ is equal to 3.44 (see Eq.(42) below). In our case, we have $n_\ell \nu'_s(n_\ell) = 35.7$, so $\nu_s(n_1)$ is sensitive to small variations of n_1 and the coefficient of n_2 in p in Eq.(40) is large in magnitude.

Furthermore, we consider equilibrium gas-liquid coexistence, where the solvent and solute densities in the bulk are n_1^g and n_2^g in gas and are n_1^ℓ and n_2^ℓ in liquid. Then, Eq.(37) gives the solute density ratio,

$$n_2^\ell/n_2^g = \exp(-\Delta\nu_s) = \exp(-\Delta\mu_s/T). \quad (41)$$

Here, $\Delta\mu_s = T\Delta\nu_s$ is the difference of the solvation chemical potential between gas and liquid [18, 57–59], which is often called the Gibbs transfer free energy (per solute particle in our case). In DFT, Eq.(38) yields

$$\Delta\nu_s = [\nu_h(n_1^\ell) - \nu_h(n_1^g)] - (n_1^\ell - n_1^g)w_{12}/T. \quad (42)$$

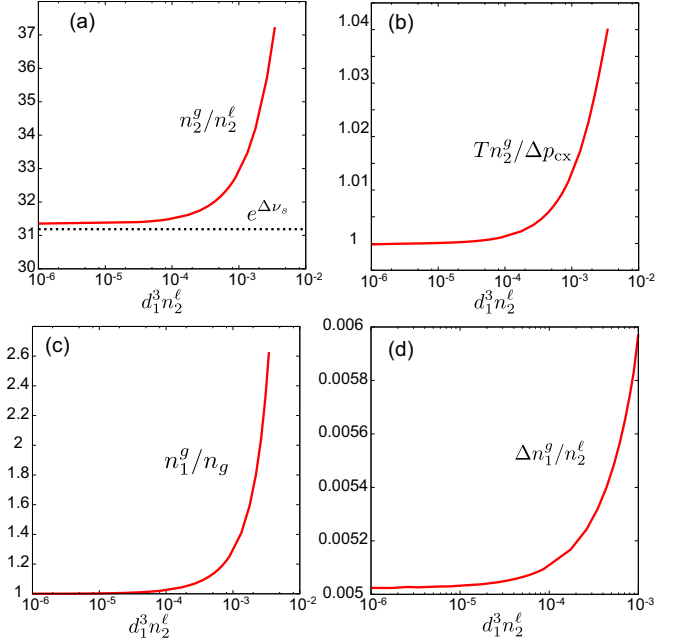


FIG. 4: Thermodynamic relations in gas-liquid coexistence in dilute binary mixtures with increasing solute density n_2^ℓ in liquid. (a) Ratio n_2^g/n_2^ℓ of solute densities in gas and liquid. Its dilute limit is 31, but it increases up to 37 at $d_1^3 n_2^\ell \sim 0.005$. (b) Ratio $T n_2^g / \Delta p_{cx}$ vs $d_1^3 n_2^\ell$, which is very close to 1 supporting Eq.(53). (c) Ratio n_1^g/n_g vs $d_1^3 n_2^\ell$, where the pure fluid limit $n_g = 2.05 \times 10^{-5} d_1^{-3}$ is very small and n_i^g remains of order n_g . (d) Ratio $\Delta n_1^g/n_2^\ell$ vs $d_1^3 n_2^\ell$, where $\Delta n_1^g = n_1^g - n_g$. It is about 0.005 in accord with Eq.(51).

Note that Eq.(41) is valid even across curved interfaces. If $n_1^\ell \gg n_1^g$, we have $\nu_s(n_1^g) \cong 0$ and $\Delta\nu_s \cong \nu_s(n_1^\ell)$. In the dilute limit of solute, we may replace n_1^g and n_1^ℓ in Eq.(42) by their pure fluid limits, n_g and n_ℓ , respectively. Then, the factor $\exp(-\Delta\nu_s)$ can be related to the Henry constant[62, 63], from which $\Delta\nu_s$ is 3.44 for O_2 and is 4.12 for N_2 in water at $T = 300$ K[15]. If $\Delta\nu_s$ is much larger, the solute tends to form solid aggregates in water as hydrophobic hydration [4–6].

Ishizaki *et al.* calculated the solvation chemical potential for Lennard-Jones systems via molecular dynamic simulation [60]. We also note that our solvation chemical potential does not account for the effect of orientational degrees of freedom in polar fluids. In particular, for water, we should investigate the effect of the hydrogen bonding on the solvation chemical potential [61].

B. Algebraic tails in density profiles

We note that the densities themselves have algebraic tails for $|z - z_{int}| \gg d_1$ [23, 54, 55], as $\Delta\Pi(z)$ in Eq.(29). For the Lennard-Jones potential in Eq.(7), Eq.(13) gives

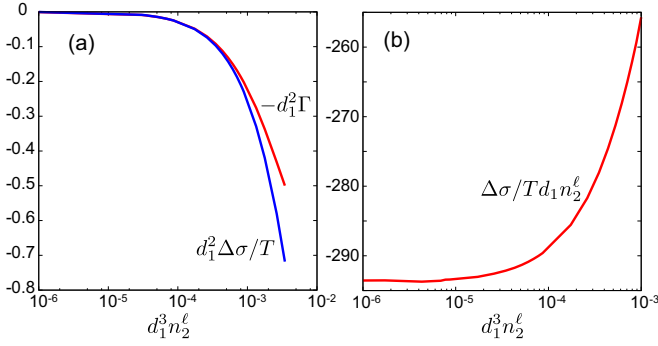


FIG. 5: Surface tension change $\Delta\sigma = \sigma - \sigma_0$ in dilute mixtures with increasing solute density in liquid n_2^ℓ . (a) $d_1^2 \Delta\sigma/T$ vs $d_1^3 n_2^\ell$, which is compared with normalized surface adsorption of solute $d_1^2 \Gamma$ (see Eq.(57)). (b) Ratio $\Delta\sigma/Td_1 n_2^\ell$ vs $d_1^3 n_2^\ell$, which is about -290 .

$$\mu_{ai} \cong \sum_j w_{ij} n_j + T A_i (z - z_{\text{int}})^{-3} \text{ with}$$

$$A_i = 2\pi \sum_j \epsilon_{ij} d_{ij}^6 (n_j^\ell - n_j^g) / 3T, \quad (43)$$

Because $\mu_i = \text{const.}$, the deviations defined by $\delta_\alpha n_i(z) \equiv n_i(z) - n_i^\alpha$ ($\alpha = g, \ell$) decay for $|z - z_{\text{int}}| \gg d_1$ as

$$\delta_\alpha n_1(z) / n_1^\alpha \cong -n_1^\alpha T K_\alpha A_1 / (z - z_{\text{int}})^3, \quad (44)$$

$$\delta_\alpha n_2(z) / n_2^\alpha \cong -\nu'_s(n_1^\alpha) \delta_\alpha n_1 - A_2 / (z - z_{\text{int}})^3. \quad (45)$$

In particular, the solute density decays in the gas side as $n_2(z) - n_2^g \sim d_1^6 n_1^\ell n_2^g |z - z_{\text{int}}|^{-3}$. We have numerically obtained these tails in excellent agreement with Eqs.(42) and (43) (not shown here).

C. Thermodynamics in gas-liquid coexistence

When gas and liquid phases are separated by a planar interface, we consider the solute-induced deviations in the bulk. For example, the coexisting (saturated vapor) pressure p_{cx} increases with increasing n_2^ℓ from its pure fluid limit p_{cx}^0 , where $p_{\text{cx}}^0 = 2.1 \times 10^{-5} p_0$ with $p_0 = T d_1^{-3}$ in our case. To linear order in n_2^α , the deviation of μ_1 and the shift $\Delta p_{\text{cx}} = p_{\text{cx}} - p_{\text{cx}}^0$ are calculated as [56]

$$\Delta\mu_1 = (n_2^\alpha K_\alpha)^{-1} \Delta n_1^\alpha + T \nu'_s(n_\alpha) n_2^\alpha, \quad (46)$$

$$\begin{aligned} \Delta p_{\text{cx}} &= (n_\alpha K_\alpha)^{-1} \Delta n_1^\alpha + T[1 + n_\alpha \nu'_s(n_\alpha)] n_2^\alpha \\ &= n_\alpha \Delta\mu_1 + T n_2^\alpha, \end{aligned} \quad (47)$$

where $\Delta n_1^\alpha = n_1^\alpha - n_\alpha$ is the solvent density deviation and K_α is the isothermal compressibility of pure solvent in phase α defined by $f_w''(n_\alpha) - w_{11} = 1/n_\alpha^2 K_\alpha$. These relations hold both for gas and liquid ($\alpha = g, \ell$). Thus,

$$\Delta\mu_1 = -T[n_2]/[n_1] = T(n_2^g - n_2^\ell)/(n_\ell - n_g), \quad (48)$$

$$\Delta n_1^\alpha = -T n_2^\alpha K_\alpha ([n_2]/[n_1] + \nu'_s(n_\alpha) n_2^\alpha). \quad (49)$$

Here, for any quantity \mathcal{A} , the difference of the values of \mathcal{A} in coexisting liquid and gas is written as $[\mathcal{A}] = \mathcal{A}_\ell - \mathcal{A}_g$.

For example, $[n_i] = n_i^\ell - n_i^g$. Dividing the second line of Eq.(47) by n_α , we also obtain the solute-induced shift of the coexisting pressure.[56],

$$\Delta p_{\text{cx}} = T \frac{[n_2/n_1]}{[1/n_1]} = T \frac{n_\ell n_2^g - n_g n_2^\ell}{n_\ell - n_g}. \quad (50)$$

In our previous paper [15] we assumed the conditions $n_\ell \gg n_g$ and $\exp(\Delta\nu_s) \gg 1$ far from the criticality, where Eqs.(49) and (50) are rewritten as

$$\Delta n_1^g \cong [1 - n_\ell \nu'_s(n_g)](n_g/n_\ell) n_2^g, \quad (51)$$

$$\Delta n_1^\ell \cong T n_\ell K_\ell [1 - e^{-\Delta\nu_s} n_\ell \nu'_s(n_\ell)] n_2^g, \quad (52)$$

$$\Delta p_{\text{cx}} \cong T n_2^g = e^{\Delta\nu_s} T n_2^\ell, \quad (53)$$

Here, Δn_1^g is much smaller than n_2^g by the factor n_g/n_ℓ in Eq.(51) and the pressure shift p_{cx} arises solely from the solute in gas for $n_2^g \gg n_1^g$ in Eq.(53). Also Δn_1^ℓ can be very small for sufficiently small $K_\ell \ll 1/n_\ell T$. In our analysis, we obtain $T n_\ell K_\ell = 0.025$, $n_\ell \nu'_s(n_g) = -7.07$, $n_\ell \nu'_s(n_\ell) = 35.7$, and $e^{-\Delta\nu_s} n_\ell \nu'_s(n_\ell) = 1.14$. Substitution of these values in Eqs.(51) and (52) yields $\Delta n_1^g \cong 1.6 \times 10^{-4} n_2^g$ and $\Delta n_1^\ell \cong -3.6 \times 10^{-3} n_2^g$. Thus, the solvent density is almost unchanged both in gas and liquid.

In Fig.4, we plot the ratios (a) n_2^g/n_2^ℓ , (b) $T n_2^g/\Delta p_{\text{cx}}$, (c) n_1^g/n_g , and (d) $\Delta n_1^g/n_2^\ell$ as functions of n_2^ℓ . In (a), the density ratio obeys Eq.(41) with $\Delta\nu_s = 3.44$ for $d_1^3 n_2^\ell \lesssim 10^{-3}$, but it increases up to 37 for larger n_2^ℓ . In (b), Eq.(53) holds for all n_2^ℓ investigated. In (c), n_1^g/n_g increases from 1 up to about 2.6 staying at very small values. In (d), Δn_1^g increases with increasing n_2^ℓ linearly as $\Delta n_1^g \cong 0.005 n_2^\ell \cong 1.6 \times 10^{-3} n_2^g$ in accord with Eq.(51).

We note that Eqs.(46)-(53) are general thermodynamic relations. Let us consider the Gibbs-Duhem relation of binary mixtures at fixed T in two-phase coexistence,

$$dp = n_1^\alpha d\mu_1 + n_2^\alpha d\mu_2, \quad (54)$$

which holds both for $\alpha = g$ and ℓ . Since $n_2 d\mu_2 \cong T dn_2$ for small n_2 , integration of Eq.(54) with respect to n_2 yields Eqs.(47)-(50).

With addition of a solute, a homogeneous liquid (without bubbles) becomes metastable against bubble formation if its pressure \bar{p} is made slightly lower than $p_{\text{cx}} = p_{\text{cx}}^0 + \Delta p_{\text{cx}}$. This condition can be realized even outside the solvent coexistence curve $\bar{p} > p_{\text{cx}}^0$ if n_2^ℓ exceeds a threshold solute density n_2^c [15] given by

$$n_2^c = e^{-\Delta\nu_s} (\bar{p} - p_{\text{cx}}^0) / T. \quad (55)$$

For $\bar{p} < p_{\text{cx}}^0$ (inside CX), bubbles can appear even without solute, so we may set $n_2^c = 0$. In ambient water with $\bar{p} - p_{\text{cx}}^0 \sim 1$ atm, n_2^c is very small even for *mildly hydrophobic* gases such as O_2 and N_2 [15].

We also examine the deviation of the surface tension $\Delta\sigma = \sigma - \sigma_0$ due to dilute solute, where σ_0 is the surface tension without solute. We consider the deviation of ω in Eq.(19), where the coefficient in front of the solute

density deviation $\Delta n_1(z)$ vanishes from the homogeneity of μ_1 [56]. To first order in n_2 , we find

$$\Delta\sigma = \int dz [\Delta p_{\text{cx}} - n_1(z)\Delta\mu_1 - Tn_2(z)]. \quad (56)$$

From Eqs.(48) and (50), we obtain the Gibbs adsorption formula $\Delta\sigma = -T\Gamma$ [27]. Here, Γ is the solute adsorption,

$$\Gamma = \int dz \left[n_2(z) - n_2^g - \frac{[n_2]}{[n_1]}(n_1(z) - n_1^g) \right]. \quad (57)$$

In Fig.1, we notice that the adsorption occurs in the gas side in (b) and (c) of Fig.1 (left of the Gibbs dividing surface), where $\Gamma = 0.132d_1^{-2}$ in (b) and $\Gamma = 0.432d_1^{-2}$ in (c). Furthermore, in Fig.5, we plot (a) $\Delta\sigma$ and Γ and (b) $\Delta\sigma/n_2^\ell$ as functions of n_2^ℓ . In addition to the Gibbs adsorption law, we can see the linear behavior $-\Delta\sigma/d_1T \cong 290n_2^\ell \cong 9.3n_2^g$ for small n_2^ℓ .

In our previous thermodynamic theory[15], we assumed a constant σ independent of the solute density. However, a decrease in σ increases the stability of small bubbles with a smaller Laplace pressure. The Gibbs law has been used for interfacial adsorption of neutral surfactants. Its generalization including the electrostatic interaction was given in our previous papers[18, 64].

D. Stable solute-induced bubbles

In our previous paper[15], we showed that small, stable bubbles minimize an appropriately defined bubble free energy for $\bar{p} > p_{\text{cx}}^0$. They are induced by a small amount of moderately hydrophobic gas in water. In contrast, in pure fluids, equilibrium bubbles with macroscopic sizes appear at fixed cell volume inside CX [31, 65]. Here, we place a spherical bubble at the center of a spherical cell, fixing the total solvent and solute numbers N_1 and N_2 . See Fig.6 for typical density profiles around stable bubbles.

1. Stress tensor around a bubble and Laplace law

In our spherically symmetric geometry, we take the reference frame with the origin at the bubble center. The average stress tensor is generally of the form[49, 53],

$$\Pi_{\alpha\beta} = p_{\parallel}(r)\delta_{\alpha\beta} - \Delta\Pi(r)(\delta_{\alpha\beta} - \hat{x}_\alpha\hat{x}_\beta), \quad (58)$$

where $\hat{\mathbf{r}} = (\hat{x}, \hat{y}, \hat{z}) = r^{-1}\mathbf{r}$. The parallel component $p_{\parallel}(r) = \sum_{\alpha\beta} \Pi_{\alpha\beta}\hat{x}_\alpha\hat{x}_\beta$ and the stress difference $\Delta\Pi(r)$ depend only on r . With Eq.(58), the mechanical equilibrium condition $\sum_{\beta} \nabla_{\beta} \Pi_{\alpha\beta} = 0$ is rewritten as

$$\frac{d}{dr}p_{\parallel}(r) = -\frac{2}{r}\Delta\Pi(r). \quad (59)$$

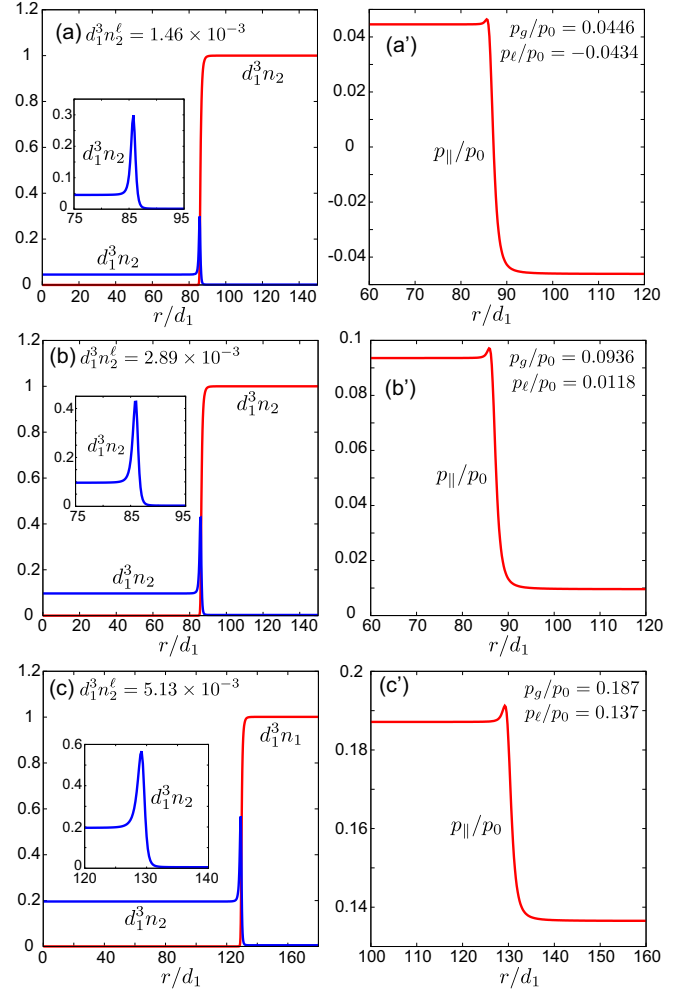


FIG. 6: Densities $n_1(r)$ and $n_2(r)$ (left) and pressure $p_{\parallel}(r)$ along $\hat{\mathbf{r}}$ (right) around stable spherical bubbles, where $d_1^3 n_2^\ell$ is (a) 1.46×10^{-3} , (b) 2.89×10^{-3} , (c) 5.13×10^{-3} , with $d_1^3 n_1^\ell \cong 1$. Pressures (p_g, p_l) in bulk gas and liquid are (a) (0.0446, -0.0434), (b) (0.0936, 0.0118), and (c) (0.187, 0.137) in units of $p_0 = T/d_1^3 = 153$ MPa, where the difference $p_g - p_l$ is close to $2\sigma/R$. Here, p_l is negative (-6 Mpa) in (a), while it is much above p_{cx}^0 for (b) and (c). Cell length L is $400d_1$ in (a) and (b) and is $800d_1$ in (c).

We assume that the bubble radius R much exceeds the molecular lengths, where it is determined by

$$R = \int_0^L dr [n_1(r) - n_1^\ell] / [n_1^g - n_1^\ell]. \quad (60)$$

We first calculate $\Delta\Pi(r)$ for $R \gg d_1$. Since $2\Delta\Pi = 3 \sum_{\alpha\beta} \Pi_{\alpha\beta} \hat{x}_\alpha \hat{x}_\beta - \sum_{\alpha} \Pi_{\alpha\alpha}$ from Eq.(58), Eq.(10) yields

$$\Delta\Pi(r) = \frac{1}{4} \int d\mathbf{r}_1 \int d\mathbf{r}_2 \sum_{ij} [r_{12} - 3(\hat{\mathbf{r}} \cdot \mathbf{r}_{12})^2 / r_{12}] \times \phi'_{ij}(r_{12}) \delta_s(\mathbf{r}, \mathbf{r}_1, \mathbf{r}_2) n_i(r_1) n_j(r_2), \quad (61)$$

where the integrand is nonvanishing only for $r_1 < r < r_2$ or $r_2 < r < r_1$ due to the δ_s function. Furthermore, if

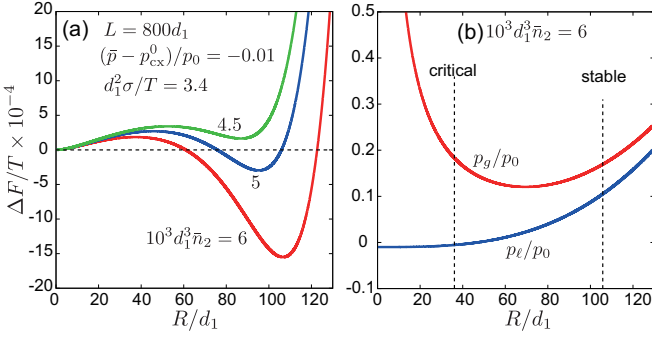


FIG. 7: (a) Bubble free energy ΔF in Eq.(65) vs R at fixed volume with $L = 800d_1$, where initial pressure is $\bar{p} = p_{cx}^0 - 0.01Td_1^{-3}$. Initial solute density is $\bar{n}_2 = 4.5, 5$, and 6 in units of $10^{-3}d_1^{-3}$ for three curves. A stable bubble is realized for the lower two curves at the minimum radius R_m . (b) Pressures inside and outside bubble p_g and p_ℓ in Eq.(65) for the lowest curve in (a). Vertical broken lines indicate critical and stable bubble radii, $R_c = 37.2d_1$ and $R_m = 106.6d_1$.

we set $u = r_{12} = |\mathbf{r}_1 - \mathbf{r}_2|$, the integrand is also non-vanishing only for $|r_1 - r_2| < u < r_1 + r_2$. Under these conditions of r_1 and r_2 , the angle integration in Eq.(61) can be performed with the aid of the relation,

$$\int d\Omega_1 \int d\Omega_2 \delta(r_{12} - u) \delta_s(\mathbf{r}, \mathbf{r}_1, \mathbf{r}_2) = \frac{4\pi u}{rr_1 r_2 W}, \quad (62)$$

where $d\Omega_i$ ($i = 1, 2$) are the solid angle elements in $d\mathbf{r}_i = dr_i r_i^2 d\Omega_i$ and $W^2 = u^4 - 2u^2(r_1^2 + r_2^2 - 2r^2) + (r_1^2 - r_2^2)^2$. For $r \gg d_1$, we may set $\hat{\mathbf{r}} \cdot \mathbf{r}_{12} \cong r_1 - r_2$ in Eq.(61) and $W \cong 2r|r_1 - r_2|$ in Eq.(62) to find

$$\Delta\Pi \cong \int_z^L dr_1 \int_0^z dr_2 \sum_{ij} \frac{\Theta_{ij}(r_1 - r_2)}{r_1 - r_2} n_i(r_1) n_j(r_2), \quad (63)$$

which is of the same form as $\Delta\Pi(z)$ in Eq.(27). Thus, $\Delta\Pi(r)$ behaves in the same manner as $\Delta\Pi(z)$ and its r -integral is equal to the surface tension σ with a correction of order R^{-1} . The Laplace law then follows if Eq.(59) is integrated across the interface at $r \cong R \gg d_1$.

In Fig.6, we display $n_1(r)$, $n_2(r)$, and $p_{||}(r)$ around stable spherical bubbles, where we calculate the densities with the method in Appendix C and $p_{||}(r)$ from Eqs.(59) and (63). Here, $d_1^3 n_2^\ell$ is (a) 1.46×10^{-3} , (b) 2.89×10^{-3} , and (c) 5.13×10^{-3} , while $d_1^3 n_1^\ell \cong 1$. The cell radius L is 400 in (a) and (b) and is 800 in (c). Remarkably, the liquid pressure p_ℓ is negative at $-0.0434p_0 = -6$ MPa in (a), while p_ℓ/p_0 is 0.0118 in (b) and 0.196 in (c). A small peak of $p_{||}$ at the interface in (b) and (c) is due to the solute adsorption. Then, R/d_1 is (a) 86.3, (b) 86.5, and (c) 129.8, while $d_1^3 \sigma/T$ is (a) 3.67, (b) 3.40, and (c) 3.06 from the integral of $\Delta\Pi$ in Eq.(63). These values yield the normalized Laplace pressure $2\sigma/Rp_0$ as (a) 0.0851, (b) 0.0786, and (c) 0.0471, in good agreement with the normalized pressure difference $(p_g - p_\ell)/p_0$ given by (a) 0.088, (b) 0.082, (c) 0.050, where $p_0 = Td_1^{-3} = 153$ MPa.

Using DFT, Talanquer *et al.*[66] calculated the density profiles of unstable critical bubbles at $R = R_c$, where the solute is accumulated in the bubble interior and its density exhibits a mild maximum at the interface. In their molecular dynamics simulation, Yamamoto and Ohnishi [67] realized stable helium-rich nanobubbles in water. They fixed the cell volume to find slightly negative pressures in the liquid region as in our Fig.6(a).

2. Equilibrium conditions and critical radius

We start with a reference (metastable) liquid state without bubbles, where the densities are $\bar{n}_i = N_i/V$ and the pressure is \bar{p} . With appearance of a single bubble at fixed cell volume, the densities in liquid are changed as

$$n_1^\ell = (1 + \phi)\bar{n}_1, \quad (64)$$

$$n_2^\ell = \bar{n}_2 - \phi n_2^g, \quad (65)$$

where $\phi = 4\pi R^3/3V$ is the bubble volume fraction. Here, we assume $\phi < \bar{n}_2/n_2^g \ll 1$. We also neglect small density heterogeneities around the bubble when it is growing or shrinking. Using the liquid compressibility K_ℓ , we write the pressures in liquid and gas as

$$p_\ell = \bar{p} + \phi/K_\ell, \quad (66)$$

$$p_g = \bar{p} + \phi/K_\ell + 2\sigma/R. \quad (67)$$

In p_ℓ we neglect the second term ($\propto n_2$) in Eq.(40), which is allowable for $n_2^g/n_\ell \ll [Tn_\ell K_\ell(1 + n_\ell \nu'_s(n_\ell))]^{-1} \cong 1$. For small K_ℓ , the compression pressure ϕ/K_ℓ can be significant even for small ϕ . For $p_g > p_{cx}^0$, the solvent density in gas n_1^g is almost unchanged from $n_g = p_{cx}^0/T$. The gas pressure is also given by $p_g = T(n_1^g + n_2^g)$, so

$$n_2^g = (\bar{p} - p_{cx}^0 + 2\sigma/R + \phi/K_\ell)/T. \quad (68)$$

If $\bar{p} < p_{cx}^0$, we require $p_{cx}^0 - \bar{p} < (8/3)(2\pi\sigma^3/K_\ell V)^{1/4} = 31.4Td_1^{-9/4}V^{-1/4}$ to ensure $n_2^g > 0$.

If we further assume the chemical balance in Eq.(41), n_2^g is also expressed as

$$n_2^g = \bar{n}_2/[e^{-\Delta\nu_s} + \phi]. \quad (69)$$

For given \bar{n}_2 and \bar{p} , Eqs.(68) and (69) constitute a closed set of equations of R . Previously [15], we solved them without ϕ/K_ℓ at fixed \bar{p} in liquid. Also in the present fixed-volume case, we obtain two solutions at $R = R_c$ and R_m for sufficiently large \bar{n}_2 , as in Fig.7(a). The larger one R_m is the radius of a stable or metastable bubble, while the smaller one R_c is the critical radius of an unstable bubble. In the limit $\phi \rightarrow 0$, R_c is written as

$$\begin{aligned} R_c &= 2\sigma/[T\bar{n}_2 e^{\Delta\nu_s} - \bar{p} + p_{cx}^0] \\ &= 2\sigma e^{-\Delta\nu_s}/T(\bar{n}_2 - n_2^c), \end{aligned} \quad (70)$$

where n_2^c is the threshold solute density in Eq.(55). Thus, solute-induced metastability is realized for $\bar{n}_2 > n_2^c$. For pure fluids, $R_c = 2\sigma/(p_{cx}^0 - \bar{p})$ inside CX [28]. Azouzi *et al.* [29] performed a nucleation experiment at negative pressures about -100 MPa.

3. Bubble free energy at fixed N_1 - N_2 - V - T

We set up a bubble free energy F_b , removing the solvent degrees of freedom. At fixed V , it is the change of the Helmholtz free energy with appearance a single bubble. Using Eqs.(64) and (66), we express it as [15]

$$F_b = V(\phi\omega_g + \omega_\ell) + S\sigma, \quad (71)$$

where $S = 4\pi R^2$, $\phi = 4\pi R^3/3V \ll 1$, and

$$\omega_g = Tn_2^g[\ln(n_2^g/\bar{n}_2) - 1 - \Delta\nu_s] + \bar{p} - p_{cx}^0, \quad (72)$$

$$\omega_\ell = T[n_2^\ell \ln(n_2^\ell/\bar{n}_2) + \phi n_2^g] + \phi^2/2K_\ell. \quad (73)$$

Here, we assume Eq.(65); then, F_b depends on n_2^g and ϕ . Against infinitesimal changes $n_2^g \rightarrow n_2^g + \delta n_2^g$ and $\phi \rightarrow \phi + \delta\phi$, the incremental change in ΔF is written as

$$\begin{aligned} \delta F_b &= VT[\ln(n_2^g/n_2^\ell) - \Delta\nu_s]\delta(n_2^g\phi) \\ &+ V[p_g - p_{cx}^0 - Tn_2^g]\delta\phi. \end{aligned} \quad (74)$$

in terms of p_g in Eq.(67). In equilibrium, F_b is minimized with respect to n_2^g and ϕ , leading to Eqs.(44) and (68).

Let us assume the mechanical equilibrium condition (68) and not the chemical one (44). Note that the former is instantaneously realized in the slow nucleation process. Then, F_b is a function of R and its derivative is given by

$$\frac{1}{S} \frac{dF_b}{dR} = \left[\ln \frac{n_2^g}{n_2^\ell} - \Delta\nu_s \right] \left[\bar{p} - p_{cx}^0 + \frac{4\sigma}{3R} + \frac{4\phi}{3K_\ell} \right], \quad (75)$$

which vanishes under Eq.(41). For sufficiently large \bar{n}_2 , $F_b(R)$ exhibits a local maximum at $R = R_c$ and a local minimum at $R = R_m (> R_c)$. Here, R_c is the critical radius expressed as in Eq.(70) in the limit $\phi \rightarrow 0$, while R_m is a stable (metastable) bubble radius for negative (positive) $F_b(R_m)$.

In Fig.7(a), we plot $F_b(R)$ in Eq.(71) vs R at $L = 800d_1$, where $\bar{n}_1 \cong 1$ and $\bar{n}_2 = 4.5, 5$, and 6 in units of $10^{-3}d_1^{-3}$ for the three curves. The initial pressure is $\bar{p} = p_{cx}^0 - 0.01p_0$. In Fig.7(b), we plot the pressures p_ℓ and p_g in Eqs.(66) and (67) vs R for the curve of the largest \bar{n}_2 in (a). The density profiles for the stable bubble in this case are close to those in Fig.6(c).

IV. DYNAMICS OF A SOLUTE-INDUCED BUBBLE

Finally, we examine bubble dynamics combining DFT and hydrodynamics. In this paper, we assume homogeneous T in the limit of fast heat conduction. This approximation is allowable for slow solute diffusion[15]. However, T becomes inhomogeneous around growing or shrinking bubbles firstly due to adiabatic heating or cooling of bubbles and secondly due to latent heat in evaporation and condensation [39–44]. We should examine these effects in future simulations.

A. Hydrodynamic equations

We consider the mass densities $\rho_i = m_i n_i$, the velocity field \mathbf{v} , and the momentum density $\mathbf{J} = \rho \mathbf{v}$, where m_1 and m_2 are the molecular masses and $\rho = \rho_1 + \rho_2$ is the total mass density. The mass conservation yields [68]

$$\frac{\partial \rho_1}{\partial t} = -\nabla \cdot (\rho_1 \mathbf{v} - \mathbf{I}), \quad (76)$$

$$\frac{\partial \rho_2}{\partial t} = -\nabla \cdot (\rho_2 \mathbf{v} + \mathbf{I}), \quad (77)$$

where \mathbf{I} is the diffusion flux of the form,

$$\mathbf{I} = -\Lambda \nabla (\mu_2/m_2 - \mu_1/m_1). \quad (78)$$

If the solute is dilute or n_2 is small, the kinetic coefficient Λ is related to the solute diffusion constant D by

$$\Lambda = Dm_2^2 n_2 / T. \quad (79)$$

Then, as $n_2 \rightarrow 0$, we have $\nabla \rho_2 \cong Tn_2^{-1} \nabla n_2$ and $\mathbf{I} \cong -D \nabla \rho_2$. Next, the momentum equation is written as

$$\begin{aligned} \frac{\partial \mathbf{J}}{\partial t} + \nabla \cdot [\rho \mathbf{v} \mathbf{v}] &= -\nabla \cdot (\overset{\leftrightarrow}{\Pi} - \overset{\leftrightarrow}{\sigma}_{\text{vis}}) - \sum_i n_i \nabla U_i \\ &= -\sum_i n_i \nabla \mu_i + \nabla \cdot \overset{\leftrightarrow}{\sigma}_{\text{vis}}. \end{aligned} \quad (80)$$

Here, $\overset{\leftrightarrow}{\Pi} = \{\Pi_{\alpha\beta}\}$ is the stress tensor in Eq.(10) determined by n_i , and U_i is the wall potential. The second line follows from Eq.(12). The $\overset{\leftrightarrow}{\sigma}_{\text{vis}} = \{\sigma_{\alpha\beta}\}$ is the viscous stress tensor of the form,

$$\sigma_{\alpha\beta} = \eta_s (\nabla_\alpha v_\beta + \nabla_\beta v_\alpha) + (\eta_b - 2\eta_s/3) (\nabla \cdot \mathbf{v}) \delta_{\alpha\beta}, \quad (81)$$

where η_s is the shear viscosity and η_b is the bulk viscosity. In the previous papers on dynamical DFT [24, 34–36], the shear viscosity was introduced to include the hydrodynamic interaction among colloidal particles.

The total free energy $\mathcal{F}_{\text{tot}} = \mathcal{F} + \mathcal{K}$ is the sum of the Helmholtz free energy functional \mathcal{F} and the fluid kinetic energy \mathcal{K} . The latter is written as

$$\mathcal{K} = \frac{1}{2} \int d\mathbf{r} \rho v^2. \quad (82)$$

If the total particle numbers $N_i = \int d\mathbf{r} n_i$ are fixed and \mathbf{v} vanishes on the boundaries, our dynamic equations yield

$$\frac{d}{dt} \mathcal{F}_{\text{tot}} = - \int d\mathbf{r} \left[\Lambda^{-1} |\mathbf{I}|^2 + \sum_{\alpha,\beta} \sigma_{\alpha\beta} \nabla_\alpha v_\beta \right] \leq 0. \quad (83)$$

Thus, at long times, a stationary state should be realized with $\nabla \mu_1 = \nabla \mu_2 = \mathbf{v} = \mathbf{0}$.

In the kinetic theory of dilute gases, η_s tends a small constant of order $(m_1 T)^{1/2} d_1^{-2}$ and η_b tends to zero in the dilute limit [69]. These density-dependences have

been confirmed in molecular dynamics simulations [70–72]. In our case, they are crucial for the hydrodynamics in bubble. Thus, we used simple extrapolation forms,

$$\eta_s/\eta_0 = 0.14 + 0.86d_1^3n, \quad (84)$$

$$\eta_b/\eta_0 = (0.02 + 0.98d_1^3n)d_1^3n, \quad (85)$$

where $n = n_1 + n_2$ and η_0 is the viscosity in liquid.

B. Numerical results after liquid decompression

1. Method

We solved the above dynamic equations in a spherical cell with radius $L = 200d_1$, where \mathbf{v} and \mathbf{I} are parallel to $\hat{\mathbf{r}} = r^{-1}\mathbf{r}$, so we may set

$$\mathbf{v} = v(r, t)\hat{\mathbf{r}}, \quad \mathbf{I} = I(r, t)\hat{\mathbf{r}}. \quad (86)$$

As the boundary condition, we assumed $v(L, t) = I(L, t) = 0$ to fix the total particle numbers in the cell. The mesh length in time integration was $0.2d_1$.

Together with the parameters in Eq.(8), we assumed $m_1 = 3 \times 10^{-23}$ g, $m_2 = (16/9)m_1$, $D = 2 \times 10^{-4}$ cm²/s, and $\eta_0 = 0.89$ cP. Using η_0 in Eqs.(84) and (85), we measure time in units of

$$\tau = m_1/d_1\eta_0 = 0.112 \text{ ps}. \quad (87)$$

Then, we have $(d_1^2m_1/\epsilon_{11})^{1/2} = 0.041\tau$ as a characteristic microscopic time and $R^2/D = 4.0 \times 10^6\tau$ as a typical diffusion time around a bubble with radius $R = 30$ nm. The wall potential was assumed to be attractive as $U_1 = -6.5T \exp(-s/1.4)$ and $U_2 = -0.5T \exp(-s/1.23)$ with $s = (L-r)/d_1$, where $L = 200d_1$ is the cell radius. Then, the wall prefers the solvent more than the solute and no surface bubble appears.

For $t < 0$, we prepared a stable bubble with radius $R_{\text{ini}} = 53.11d_1$ with the initial densities $n_1^g = 8.37 \times 10^{-5}$, $n_1^\ell = 1.00$, $n_2^g = 0.207$, and $n_2^\ell = 5.68 \times 10^{-3}$ in units of d_1^{-3} . At $t = 0$, we suddenly decreased the liquid density n_1^ℓ in the region $r > R_{\text{ini}}$ to $0.900d_1^{-3}$, which gave rise to a negative liquid pressure about $-2.73p_0 = -419$ MPa (in a very short time). Then, the bubble expanded exhibiting a damped oscillation. At $t = 5000\tau$, the bubble radius became close to the final radius $R_\infty = 98.52d_1$, but the solute density in gas n_2^g was $0.040d_1^{-3}$ and was still noticeably smaller than the final value $0.060d_1^{-3}$. Note that the final equilibrium state can be realized with the method in Appendix C.

Our initial condition and the isothermal assumption are rather unrealistic, but the resultant dynamical processes are dramatic, providing fundamental information on the nonlinear bubble dynamics in confined geometries.

2. Acoustic disturbances

In Fig.8, we show the profiles of the solvent density $n_1(r, t)$ outside the oscillating bubble at consecutive

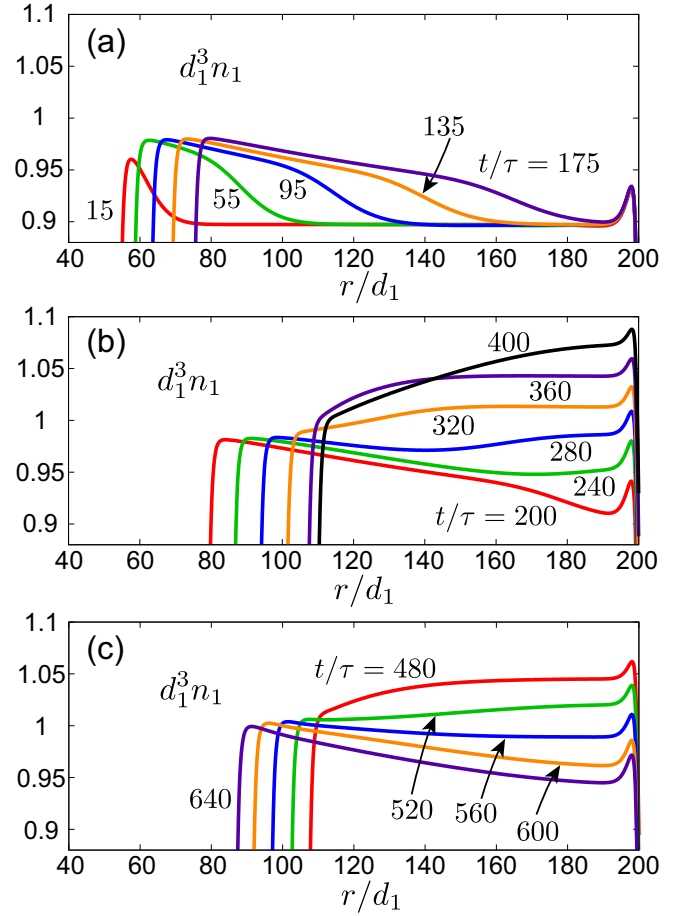


FIG. 8: Time-evolution of solvent density $n_1(r, t)$ outside a bubble with time-dependent radius $R(t)$ after decompression of liquid in a cell with $L = 200$. (a) The bubble expands emitting a large-amplitude sound outward. (b) Stepwise sound reaches the cell boundary, while the bubble is still expanding. (c) The bubble is shrinking, which causes a large decrease of $n_1(r, t)$ in liquid.

times. In (a), a large-amplitude acoustic wave is emitted in a stepwise form from the bubble surface. Its expanding speed is given by the (isothermal) sound velocity $c_\ell = \sqrt{(\partial p/\partial \rho)_T} = 0.88d_1/\tau$, which is larger than the maximum bubble expanding speed about $0.2(d_1/\tau)$. Its amplitude is gradually decreases away from the bubble, being proportional to r^{-1} in this spherically symmetric geometry. In (b), the wave reaches the cell boundary and n_1 increases near the wall. In (c), the bubble shrinks, causing an overall density decrease in the liquid region.

In Fig.9, we also show the profiles of the solute density $n_2(r, t)$ at consecutive times, which is appreciable in the bubble and has an adsorption peak. The solvent density $n_1(r, t)$ remains of order $10^{-5} - 10^{-4}d_1^{-3}$ in the bubble. In (a), the outward interface motion gives rise to a negative stepwise wave propagating inward with the sound speed $c_g = (T/m_2)^{1/2} = 0.14d_1/\tau$. Here, the acoustic traversal time R/c_g is about 880τ and is close to the oscillation period 650τ . In (b), $n_2(r, t)$ still changes inhomogeneously

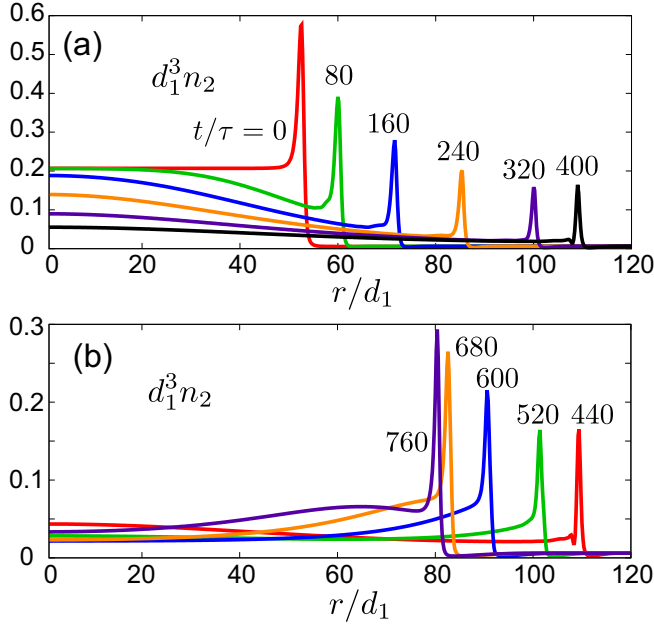


FIG. 9: Time-evolution of solute density $n_2(r,t)$ inside a bubble during its expansion in (a) and its shrinkage in (b). Outward and inward interface motions propagate as acoustic waves. The sound speed is of the same order as the interface velocity. In (b), scale of the vertical axis is twice enlarged.

during the bubble shrinkage. However, it becomes gradually homogeneous after several oscillations. If we would use liquid viscosities in the bubble, we would have uniform dilation with $v_i \propto x_i$ from the early stage. It is worth noting that the bubble interior has been assumed to be homogeneous in the literature [42–45]. In addition, we notice that the adsorption Γ in our case noticeably depends on time (see Fig.13(d) and its explanation).

3. Damped oscillation

In Fig.10, we examine early-stage time-evolution in the range $0 < t < 5000\tau = 560$ ps. The bubble radius undergoes a damped oscillation and approaches the final value $98.52d_1$, while the particle transport through the interface was negligible. The period is about 650τ and the damping rate is about $5.1 \times 10^{-4}\tau^{-1}$. We display (a) the bubble radius $R(t)$, which is defined as the peak position of $n_2(r,t)$ in our nonequilibrium situation (see Fig.9). In (b), we plot the liquid pressure $p_\ell(t)$ (taken at $r = 170d_1$) and the gas pressure $p_g(t)$ (taken at $r = 2d_1$), where the former exhibits a large damped oscillation but the latter variation is much smaller. The Laplace relation does not hold during the bubble oscillation. In (c), we show the solute density $n_2^g(t)$ and the total solute number within the bubble defined by $N_2^b(t) = \int_{r < R} dr n_2(r,t)$. Here, $n_2^g(t)$ largely oscillates, but $N_2^b(t)$ weakly increases only by a few %. This implies that the solute transport through the interface is small and $n_2^g(t) \sim R(t)^{-3}$ in this time

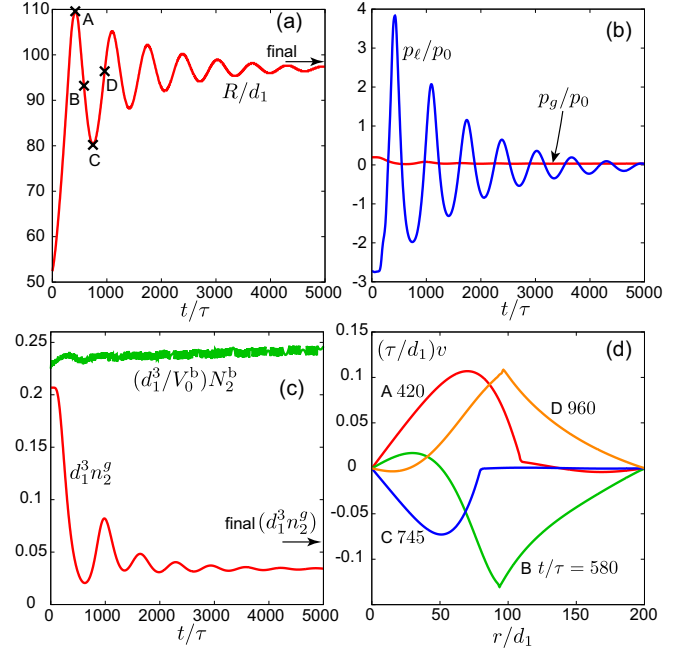


FIG. 10: Early-stage time-evolution ($0 < t < 5000\tau$). (a) Bubble radius $R(t)$, which approaches the final radius (arrow). (b) Liquid pressure $p_\ell(t)$ at $r = 170d_1$ and gas pressure $p_g(t)$ at $r = 2d_1$ divided by $p_0 = Td_1^{-3}$, where p_ℓ exhibits a large damped oscillation but $p_g \cong Tn_2^g$ is much smaller. (c) $d_1^3 n_2^g(t)$ exhibiting a damped oscillation, which is noticeably smaller than the final value (arrow). Total inter-bubble solute number N_2^b is very slowly increasing, so $n_2^g(t)$ is nearly proportional to $R(t)^{-3}$. (d) Velocity profiles in the radial direction $v(r,t)$ divided by d_1/τ in the cell, where t/τ is (A) 428, (B) 580, (C) 745, and (D) 980. The corresponding times are marked in (a).

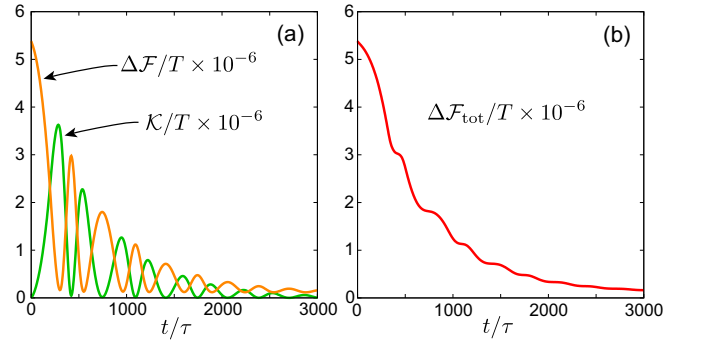


FIG. 11: (a) DFT free energy deviation $\Delta\mathcal{F}(t) = \mathcal{F}(t) - \mathcal{F}(\infty)$ and kinetic energy $\mathcal{K}(t)$ vs t/τ . (b) Their sum $\mathcal{F}_{\text{tot}}(t)$. Here, $\Delta\mathcal{F}(t)$ and $\mathcal{K}(t)$ exhibit a damped oscillation, but $\mathcal{F}_{\text{tot}}(t)$ decreases monotonically in time.

region. In addition, in (d), we show the profiles of the radial velocity $v(r,t)$ at four characteristic times.

In Fig.11, the kinetic energy $\mathcal{K}(t)$ in Eq.(82) and the DFT free energy deviation $\Delta\mathcal{F}(t) = \mathcal{F}(t) - \mathcal{F}_\infty$ undergo damped oscillations out of phase with each other, where \mathcal{F}_∞ is the final value of \mathcal{F} . However, their sum

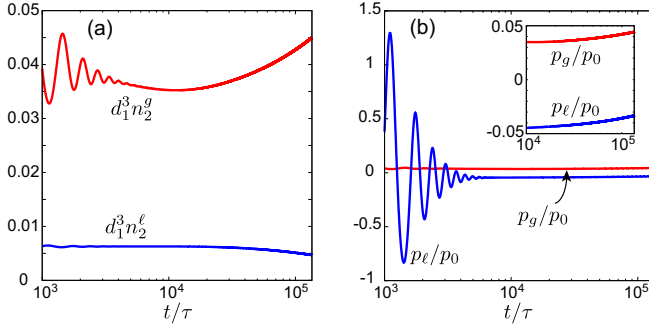


FIG. 12: Long-time evolution ($t < 1.3 \times 10^5 \tau$). (a) $d_1^3 n_2^g(t)$ and $d_1^3 n_2^l(t)$ vs t/τ . For $t \gtrsim 10^4 \tau$, $n_2^g(t)$ increases and $n_2^l(t)$ decreases slowly due to a solute flux into the bubble. (b) $p_l(t)/p_0$ and $p_g(t)/p_0$. Laplace law holds after the damped oscillation. They increase very slowly for $t \gtrsim 10^4 \tau$ (inset) due to a small increase in $R(t)$.

$\Delta \mathcal{F}_{\text{tot}}(t) = \mathcal{K}(t) + \Delta \mathcal{F}(t)$ decreases monotonically in time in accord with Eq.(83). Indeed, the radius deviation δR from the mean radius (slightly smaller than R_∞) approximately obeys

$$M \ddot{R} = -k \delta R - \zeta \dot{R}. \quad (88)$$

where $\dot{R} = d\delta R/dt$ and $\ddot{R} = d^2\delta R/dt^2$. We estimate ζ from $d\Delta \mathcal{F}/dt = -\zeta \dot{R}^2$, k/M from the oscillation period, and M from $M = 2\mathcal{K}/\dot{R}^2$. Then, $M = 3.9\rho R_\infty^3$, $k = 2.1L/K_\ell$, and $\zeta = 51\eta_0 R_\infty$. Here, $\Delta \mathcal{F}$ arises from the change in the liquid volume, while it is given by the surface free energy ($\sim 4\pi\sigma R^2$) for $L \gg R$ [42–45].

4. Long-time behavior

For $t > 5000\tau$, the bubble radius $R(t)$ is close to the final one R_∞ , but small $n_2(r, t)$ still evolves diffusively in the liquid region. The final state should be reached on a timescale of $10^7 \tau$. In our case, $K_\ell \cong 0.025/Tn_1^\ell$ and $L \cong 2R$, so that the compression pressure $\phi/K_\ell \sim 5p_0$ is much larger than the Laplace one $2\sigma/R \sim 0.1p_0$, where $p_0 = Td_1^{-3}$. Moreover, from Eq.(40), the small pressure deviation remaining in bulk liquid is written as

$$\frac{p - p_\infty}{p_0} = B_1[n_1(r, t) - n_{1\infty}] + B_2[n_2(r, t) - n_{2\infty}], \quad (89)$$

where p_∞ , $n_{1\infty}$, and $n_{2\infty}$ are the final homogeneous values of p , n_1 , and n_2 in liquid, respectively, $B_1 = 1/TK_\ell = 40.0d_1^3$, and $B_2 = d_1^3[1 + n_1\nu'_s(n_1)] = 36.7d_1^3$. Since p should be homogeneous in liquid without sounds, this relation indicates that weak inhomogeneity of n_1 should be induced by that of n_2 in liquid.

In Fig.12, we plot $n_2^g(t)$ at $r = 2d_1$ and $n_2^l(t)$ at $r = 170d_1$ for $t < 2 \times 10^5 \tau$. In (a), we can see a slow increase in $n_2^g(t)$ and a slow decrease in $n_2^l(t)$ for $t \gtrsim 10^4 \tau$, due to the solute transport into the bubble. In (b), $p_\ell(t)$

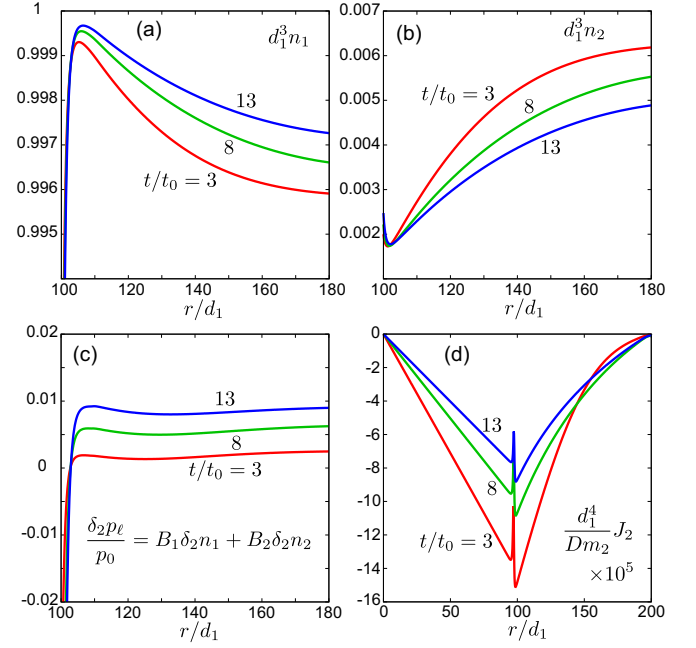


FIG. 13: Profiles at $t/t_0 = 3, 8$, and 13 with $t_0 = 10^4 \tau$. (a) $d_1^3 n_1(r, t)$ and (b) $d_1^3 n_2(r, t)$ in liquid. (c) Linear combination $\delta_2 p_\ell/p_0 \equiv B_1 \delta_2 n_1 + B_2 \delta_2 n_2$, where $\delta_2 n_i \equiv n_i(r, t + t_0) - n_i(r, t_0)$ with $B_1 = 40.0d_1^3$ and $B_2 = 36.7d_1^3$. Here, $\delta_2 p_\ell$ is equal to the pressure change $p(r, t + t_0) - p(r, t_0)$ from Eq.(40) and is homogeneous away from the interface. (d) Solute flux $J_2 = \rho_2 v + I(r, t)$ multiplied by $10^5 d_1^4 / Dm_2$.

and $p_g(t)$ satisfy the Laplace law after the damped oscillation. For $t \gtrsim 10^4 \tau$, they increase slowly with the fixed difference, because of a small increase in R . Here, R increases by $0.3d_1$ in time interval $[3t_0, 13t_0]$, producing a compressional pressure increase about $0.0135p_0$.

In Fig.13, we display profiles at $t/t_0 = 3, 8$, and 13 with $t_0 = 10^4 \tau$. In (a), $n_1(r, t)$ exhibits inhomogeneity in accord with Eq.(89). Its overall increase is induced by the above-mentioned small increase in R . In (b), $n_2(r, t)$ relaxes diffusively far from the interface. In (c), we examine the incremental changes $\delta_2 p_\ell \equiv p(r, t + t_0) - p(r, t_0)$ and $\delta_2 n_i \equiv n_i(r, t + t_0) - n_i(r, t_0)$ in time interval $[t_0, t_0 + t]$. Then, the linear combination $\delta_2 p_\ell/p_0 \equiv B_1 \delta_2 n_1 + B_2 \delta_2 n_2$ is surely homogeneous far from the interface.

In Fig.13(d), we display the solute flux $J_2(r, t) = \rho_2 v + I$ in the radial direction (see Eq.(86)). Here, v is nonvanishing only in the bubble interior, where $\rho_2 = m_2 n_2$ is uniform so that the gas is dilated by

$$v(r, t) = (\dot{R}/R)r. \quad (90)$$

At the interface $r = R$ (defined as the peak position of $n_2(r, t)$), $J_2(r, t)$ is slightly discontinuous across the peak of $n_2(r, t)$. This discontinuity gives rise to a change in the surface adsorption $\Gamma(t)$ in Eq.(57) as

$$\frac{d}{dt}\Gamma(t) = \frac{1}{m_2}[J_2(R-0, t) - J_2(R+0, t)]. \quad (91)$$

In (d), the right hand side is of order $10^{-5}D/d_1^4 = 2.5 \times 10^{-7}/d_1^2\tau$. In accord with this, $d_1^2\Gamma$ is 0.169, 0.185, and 0.211 at $t/t_0 = 3, 8$, and 13, respectively, which indeed leads to $d\Gamma/dt \cong 3 \times 10^{-7}/d_1^2\tau$.

V. SUMMARY AND REMARKS

We have investigated statics and dynamics of phase separated states induced by a neutral low-density solute using DFT. At fixed $T = 300$ K, we have assumed a considerably large solvation chemical potential $T\nu_s$ in liquid and a relatively weak solute-solute attractive interaction, under which small bubbles can appear in equilibrium[15–17]. Main results in this paper are as follows.

(i) In Sec.II, we have presented some general relations in DFT for the stress tensor $\Pi_{\alpha\beta}$ in Eqs.(12), (15), and (19) and for the surface tension in Eqs.(21) and (25). The interface profiles of the densities $n_i(z)$ and the stress difference $\Delta\Pi(z) = \Pi_{zz} - \Pi_{xx}$ have been calculated in Fig.1. These quantities have algebraic tails away from the interface ($\propto |z - z_{\text{int}}|^{-3}$ for Lennard-Jones potentials as in Fig.2). In particular, we have shown that the derivative $d\Delta\Pi/dz$ can be expressed in simple forms in DFT and in the exact statistical theory (Appendix B).

(iii) In Sec.III, we have calculated the solvation chemical potential $\mu_s = T\nu_s$ using the binary Carnahan-Starling model[26] in the dilute limit, as plotted in Fig.3. We have then calculated solute-induced deviations, such as the shift of the coexisting pressure Δp_{cx} , in gas-liquid coexistence for dilute binary mixtures. We have also found small solute-rich bubbles, which are stable because they minimize the free energy functional of DFT. We have calculated the interface profiles of the densities and $\Delta\Pi$ for such bubbles in Fig.6.

(iv) In Sec.IV, we have investigated bubble dynamics using dynamic equations where DFT and the hydrodynamics are combined. We have described a damped oscillation with acoustic disturbances and a subsequent solute diffusion after a sudden decompression. In the late stage, weak solvent inhomogeneity is also induced such that the liquid pressure becomes homogeneous as in Fig.13.

We make some remarks. (1) We should calculate the profiles of surface bubbles on a wall in various conditions. The dewetting transition should be sensitive to a small amount of a solute (hydrophobic one for water)[17]. Bridging of two closely separated walls or colloidal particles by bubbles is also of great importance [14, 16, 17]. (2) In our analysis, the solute is mildly adsorbed at the interface due to a minimum of $\nu_s(n_1)$ in Eq.(38). More dramatic effects of adsorption should emerge with addition of surfactants and/or ions in the bubble formation. They are usually present in real water. (3) Bubble collapse after a pressure increase is also worth studying. In bubble dynamics, we will include inhomogeneous T

due to adiabatic density changes and latent heat in the scheme of the dynamic van der Waals theory [37, 39–41].

Acknowledgments

This work was supported by KAKENHI No.25610122. One of the authors (R. O.) acknowledges support from the Grant-in-Aid for Scientific Research on Innovative Areas "Fluctuation and Structure" from the Ministry of Education, Culture, Sports, Science, and Technology of Japan.

Appendix A: Binary Carnahan-Starling model

In the binary Carnahan-Starling model[26], the volume fractions of the two species are

$$\eta_i = v_{0i}n_i, \quad v_{0i} = \pi d_{ii}^3/6 \quad (i = 1, 2). \quad (\text{A1})$$

The repulsive part of the free energy density f_h in Eq.(1) is written as a function of the total volume fraction $\eta = \eta_1 + \eta_2$. We here rewrite it in terms of $u = \eta/(1 - \eta)$ as

$$\frac{f_h}{nT} = 4u + u^2 - \frac{3}{2}u[2y_1 + (y_1 + y_2)u] + (y_3 - 1)g(u). \quad (\text{A2})$$

The parameters y_1 , y_2 , and y_3 depend on n_1 and n_2 as

$$y_1 = (1 + \alpha)(1 - \alpha)^2 n_1 n_2 / n(n_1 + \alpha^3 n_2), \quad (\text{A3})$$

$$y_2/y_1 = \alpha(n_1 + \alpha^2 n_2) / (1 + \alpha)(n_1 + \alpha^3 n_2), \quad (\text{A4})$$

$$y_3 = [n_1 + \alpha^2 n_2]^3 / n(n_1 + \alpha^3 n_2)^2, \quad (\text{A5})$$

where $n = n_1 + n_2$. In the one-component limit ($n_2 \rightarrow 0$)[25], we have $y_1 = y_2 = y_3 - 1 = 0$. The function $g(u)$ in the last term in Eq.(A2) depends on u as

$$g(u) = u - u^2/2 - \ln(1 + u). \quad (\text{A6})$$

The pressure p_h from f_h in Eq.(9) is written as

$$\begin{aligned} \frac{p_h}{Tn} &= (u + u^2)[4 + 2u - 3y_1 - 3(y_1 + y_2)u] + (1 - y_3)u^3 \\ &= \frac{1 + \eta + \eta^2}{(1 - \eta)^3} - \frac{3(y_1 + y_2\eta)\eta + y_3\eta^3}{(1 - \eta)^3} - 1. \end{aligned} \quad (\text{A7})$$

The chemical potential contributions $\mu_{hi} = \partial f_h / \partial n_i$ from f_h in Eq.(6) are written as

$$\mu_{h1} = f_h/n - X_1 + v_{01}p_h/\eta, \quad (\text{A8})$$

$$\mu_{h2} = f_h/n + n_1 X_1/n_2 + v_{02}p_h/\eta, \quad (\text{A9})$$

where $v_{0i} = \pi d_{ii}^3/6$. In terms of the derivatives $Y_i = \partial y_i / \partial n_1$ at fixed n_2 , X_1 is written as

$$X_1 = Tn[3u[Y_1 + (Y_1 + Y_2)u]/2 - Y_3g(u)]. \quad (\text{A10})$$

For small n_2 we have $y_1 \cong (1 + \alpha)(1 - \alpha)^2 n_2/n$, $y_2 \cong \alpha(1 + \alpha)^2 n_2/n$, and $y_3 - 1 \cong (3\alpha^2 - 2\alpha^3 - 1)n_2/n$ to linear order in n_2 . From Eq.(A2), f_h is then expanded as

$$f_h(n_1, n_2) = Tn_1(4u_1 + u_1^2) + Tn_2\nu_h(n_1) + \dots, \quad (\text{A11})$$

where $u_1 = \eta_1/(1 - \eta_1)$ and ν_h is given in Eq.(33).

Appendix B: Statistical-mechanical theory of surface tension and interfacial stress

We consider binary particle systems with pairwise interactions, where the potential $\varphi_{ij}(r)$ includes attractive and repulsive parts. A planar interface is placed perpendicularly to the z axis away from the walls at $z = 0$ and L . Then, the average stress tensor can be expressed exactly as [31, 47–49]

$$\Pi_{\alpha\beta}(\mathbf{r}) = Tn\delta_{\alpha\beta} - \int d\mathbf{r}_1 \int d\mathbf{r}_2 \sum_{ij} \frac{x_{12\alpha}x_{12\beta}}{2r_{12}} \times \varphi'_{ij}(r_{12})\delta_s(\mathbf{r}, \mathbf{r}_1, \mathbf{r}_2)\rho_2(\mathbf{r}_1, \mathbf{r}_2), \quad (\text{B1})$$

in terms of the δ_s function in Eq.(11). This expression is analogous to that of DFT in Eq.(10). We introduce the two-body distribution function,

$$\rho_{ij}(\mathbf{r}_1, \mathbf{r}_2) = \left\langle \sum_{k \neq \ell} \delta(\mathbf{r}_1 - \mathbf{R}_k^i) \delta(\mathbf{r}_2 - \mathbf{R}_\ell^j) \right\rangle, \quad (\text{B2})$$

where \mathbf{R}_k^i is the position of particle k of species i . In Eq.(B1), the kinetic part $Tn\delta_{\alpha\beta}$ arises from the Maxwell-Boltzman distribution, while the second term holds even in nonequilibrium. Around a planar interface, we may set $\rho_{ij}(\mathbf{r}_1, \mathbf{r}_2) = \rho_{ij}(z_1, z_2, r_{12})$ in equilibrium.

The surface tension is given by the Bakker formula in Eq.(25). After integration with respect to z , x_1 , and y_1 , we may remove the δ_s function to obtain the Kirkwood-Buff formula [22, 48, 49, 53],

$$\sigma = \int dz_1 \int d\mathbf{r}_2 \sum_{ij} \frac{r_{12}^2 - 3z_{12}^2}{4r_{12}} \varphi'_{ij}(r_{12})\rho_{ij}(\mathbf{r}_1, \mathbf{r}_2). \quad (\text{B3})$$

We also consider the stress difference $\Delta\Pi(z) = \Pi_{zz} - \Pi_{xx}$ itself. Starting with Eq.(B1) we find

$$\Delta\Pi(z) = \pi \int_z^L dz_1 \int_0^z dz_2 \int_{z_{12}}^\infty du \sum_{ij} (u^2/z_{12} - 3z_{12})$$

$$\times \varphi'_{ij}(u)\rho_{ij}(z_1, z_2, u), \quad (\text{B4})$$

where $z_1 > z > z_2$ and $z_{12} = z_1 - z_2$. Use has been made of Eq.(18) and the relation $\int dx_2 dy_2 \delta(u - r_{12}) = 2\pi u \theta(u - |z_{12}|)$ at fixed u and z_{12} . The σ in Eq.(B3) and the z integral of Eq.(B4) coincide. Analogously to Eq.(28), the derivative $d\Delta\Pi/dz$ can be written in the double integral form,

$$\frac{d}{dz} \Delta\Pi(z) = \pi \int_0^\infty d\xi \int_\xi^\infty du \sum_{ij} (u^2/\xi - 3\xi) \varphi'_{ij}(u) \times [\rho_{ij}(z + \xi, z, u) - \rho_{ij}(z - \xi, z, u)]. \quad (\text{B5})$$

Here, if $z - z_{\text{int}} \gg d_1$ and $\xi - z + z_{\text{int}} \gg d_1$, we can neglect the pair correlation at the two points and are allowed to replace $\rho_{ij}(z + \xi, z, u) - \rho_{ij}(z - \xi, z, u)$ by $(n_i^\ell - n_i^g)n_j^\ell \theta(\xi - z)$. Then, we obtain the tail in Eq.(29) if $\varphi_{ij}(r) \propto r^{-6}$ at long distances. If we replace $\varphi'_{ij}(r_{12})\rho_{ij}(\mathbf{r}_1, \mathbf{r}_2)$ in Eqs.(B3)-(B5) by $\phi'_{ij}(r_{12})n_i(z_1)n_j(z_2)$ and Tn in Eq.(B1) by $Tn + p_h$, we obtain their counterparts in DFT.

Appendix C: Efficient method of calculating equilibrium states in DFT

As a method of minimizing the free energy \mathcal{F} , we seek a stationary solution of the relaxation equations ($i = 1, 2$),

$$\frac{\partial}{\partial \tau} n_i(\mathbf{r}, \tau) = -\mu_i(\mathbf{r}, \tau) + \langle \mu_i \rangle_{\text{cell}}(\tau), \quad (\text{C1})$$

where μ_i is the chemical potential in Eq.(5) determined by $n_1(\mathbf{r}, \tau)$ and $\langle \mu_i \rangle_{\text{cell}} = \int d\mathbf{r} \mu_i/V$ is its space average in the cell. For any initial $n_i(\mathbf{r}, 0)$, $\mu_i(\mathbf{r}, \tau)$ tend to be homogeneous as $\tau \rightarrow \infty$. Then, we obtain an equilibrium state with $n_i(\mathbf{r}) = \lim_{\tau \rightarrow \infty} n_i(\mathbf{r}, \tau)$. We assume the one-dimensional geometry in Fig.1 and the spherically symmetric geometry in Fig.6. Note that there is no physical meaning in this relaxation dynamics.

-
- [1] C. N. Likos, Phys. Rep. **348**, 267 (2001).
 - [2] J. Dzubiella and J.-P. Hansen, J. Chem. Phys. **121**, 5514 (2004).
 - [3] P. Hopkins, A. J. Archer, and R. Evans, J. Chem. Phys. **131**, 124704 (2009).
 - [4] H.S. Ashbaugh and M. E. Paulaitis, J. Am. Chem. Soc. **123**, 10721 (2001).
 - [5] D. Chandler, Nature, **437**, 640 (2005).
 - [6] S. Rajamani, T.M. Truskett, and S. Garde, Proc. Natl. Acad. Sci. U.S.A. **102**, 9475 (2005).
 - [7] D. Beysens and D. Esteve, Phys. Rev. Lett. **54**, 2123 (1985).
 - [8] D. Beysens and T. Narayanan, J. Stat. Phys. **95**, 997 (1999).
 - [9] F. Schlesener, A. Hanke, and S. Dietrich, J. Stat. Phys. **110**, 981 (2003).
 - [10] R. Okamoto and A. Onuki, Phys. Rev. E **88**, 022309 (2013).
 - [11] H. Tanaka and T. Araki, Chem. Eng. Sci. **61**, 2108 (2006).
 - [12] T. Araki and H. Tanaka, J. Phys.: Condens. Matter, **20**, 072101 (2008).
 - [13] A. Furukawa, A. Gambassi, S. Dietrich, and H. Tanaka, Phys. Rev. Lett. **111**, 055701 (2013).
 - [14] S. Yabunaka, R. Okamoto, and A. Onuki, Soft Matter **11**, 5738 (2015).
 - [15] R. Okamoto and A. Onuki, Eur. Phys. J. E **38**, 72 (2015).
 - [16] P. Attard, M. P. Moody, and J.W.G. Tyrrell, Physica A **314**, 696 (2002).

- [17] J. R. T. Seddon, D. Lohse, W. A. Ducker, and V. S. J. Craig, *Chem. Phys. Chem.* **13**, 2179 (2012).
- [18] A. Onuki, R. Okamoto, and T. Araki, *Bull. Chem. Soc. Jpn.* **84**, 569 (2011).
- [19] A.F. Kostko, M.A. Anisimov, J.V. Sengers, *Phys. Rev. E* **70**, 026118 (2004).
- [20] R. Okamoto and A. Onuki, *Phys. Rev. E* **82**, 051501 (2010).
- [21] D. E. Sullivan, *Phys. Rev. B* **20**, 3991 (1979).
- [22] R. Evans, *Adv. Phys.* **28**, 143 (1979).
- [23] P. Tarazona and R. Evans, *Mol. Phys.* **48**, 799 (1983).
- [24] J. F. Lutsko, *Adv. Chem. Phys.* **144**, 1 (2010).
- [25] N. F. Carnahan and K. E. Starling, *J. Chem. Phys.* **51**, 635 (1969).
- [26] G. A. Mansoori, N. F. Carnahan, K. E. Starling, and T. W. Leland, *J. Chem. Phys.* **54**, 1523 (1971).
- [27] J. W. Gibbs, *Collected Works* (Yale University Press, New Haven, CT, 1957), Vol. 1, pp. 219-331.
- [28] M. Blander and J. Katz, *AIChE J.* **21**, 833 (1975).
- [29] M. E. M. Azouzi, C. Ramboz, J.-F. Lenain, and F. Caupin, *Nat. Phys.* **9**, 38 (2013).
- [30] J. S. Langer and A. J. Schwartz, *Phys. Rev. A* **21**, 948 (1980).
- [31] A. Onuki, *Phase Transition Dynamics* (Cambridge University Press, Cambridge, 2002).
- [32] U. M. B. Marconi and P. Tarazona, *J. Chem. Phys.* **110**, 8032 (1999).
- [33] A. J. Archer and R. Evans, *J. Chem. Phys.* **121**, 4246 (2004).
- [34] M. Rex and H. Löwen, *Eur. Phys. J. E* **28**, 139 (2009).
- [35] B. D. Goddard, A. Nold, N. Savva, G. A. Pavliotis, and S. Kalliadasis, *Phys. Rev. Lett.* **109**, 120603 (2012).
- [36] A. Donev and E. Vanden-Eijnden, *J. Chem. Phys.* **140**, 234115 (2014).
- [37] A. Onuki, *Phys. Rev. E* **75**, 036304 (2007).
- [38] J. D. van der Waals, *Verh.-K. Ned. Akad. Wet., Afd. Natuurkd., Eerste Reeks* **1**(8), 56 (1893); English translation in : J. S. Rowlinson, *J. Stat. Phys.* **20**, 197 (1979).
- [39] R. Teshigawara and A. Onuki, *Europhys. Lett.* **84**, 36003 (2008).
- [40] R. Teshigawara and A. Onuki, *Phys. Rev. E* **82**, 021603 (2010).
- [41] R. Teshigawara and A. Onuki, *Phys. Rev. E* **84**, 041602 (2011).
- [42] M. S. Plesset and A. Prosperetti, *Ann. Rev. Fluid Mech.* **9**, 145 (1977).
- [43] M. M. Fyrillas and A. J. Szeri, *J. Fluid Mech.* **277**, 381 (1994).
- [44] E. A. Neppiras, *Phys. Rep.* **61**, 159 (1980).
- [45] M. P. Brenner, S. Hilgenfeldt, and D. Lohse, *Rev. Mod. Phys.* **74**, 426 (2002).
- [46] J. W. Cahn, *J. Chem. Phys.* **66**, 3667 (1977).
- [47] J. H. Irving and J. G. Kirkwood, *J. Chem. Phys.* **18**, 817 (1949).
- [48] J.G. Kirkwood and F. P. Buff, *J. Chem. Phys.* **17**, 338 (1949).
- [49] P. Schofield, J. R. Henderson *Proc. R. Soc. Lond. A* **379**, 231 (1982).
- [50] F. P. Buff, R. A. Lovett, and F. H. Stillinger, *Phys. Rev. Lett.* **15**, 621 (1965).
- [51] A. E. Ismail, G. S. Grest, and M. J. Stevens, *J. Chem. Phys.* **125**, 014702 (2006).
- [52] G. Bakker, in: *WIEN-HARMS' Handbuch der Experimentalphysik VI*. Leipzig: Akademische Verlagsgesellschaft 1928.
- [53] S. Ono and S. Kondo, *Molecular Theory of Surface Tension in Liquids* (Springer, Berlin, 1960).
- [54] J. A. Barker and J. R. Henderson *J. Chem. Phys.* **76**, 6303 (1982).
- [55] J.A. Stbvang, T. Aukrust, and E.H. Hauge, *Physica A* **143**, 40 (1987).
- [56] A. Onuki, *J. Chem. Phys.* **130**, 124703 (2009).
- [57] A. Ben-Naim and Y. Marcus, *J. Chem. Phys.* **81**, 2016 (1984).
- [58] B. Guillot B. and Y. Guissani, *J. Chem. Phys.* **99**, 8075 (1993).
- [59] G. Hummer, S. Garde, A. E. Garcia, and L. R. Pratt, *Chem. Phys.* **258**, 349 (2000).
- [60] M. Ishizaki, H. Tanaka, and K. Koga, *Phys. Chem. Chem. Phys.* **13**, 2328 (2011).
- [61] S. Zhao, R. Ramirez, R. Vuilleumier, and D. Borgis, *J. Chem. Phys.* **134**, 194102 (2011).
- [62] R. Sander, *Atmos. Chem. Phys. Discuss.* **14**, 29615 (2014).
- [63] F. L. Smith and A. H. Harvey, *Chemical Engineering Progress, AIChE*, **103**, 33 (2007).
- [64] A. Onuki, *EPL* **82**, 58002 (2008).
- [65] K. Binder, *Physica A* **319**, 99 (2003).
- [66] V. Talanquer, C. Cunningham, and D. W. Oxtoby, *J. Chem. Phys.* **114**, 6759 (2001).
- [67] T. Yamamoto and S. Ohnishi, *Phys. Chem. Chem. Phys.* **13**, 16142 (2011).
- [68] L.D. Landau and E.M. Lifshitz, *Fluid Mechanics* (Pergamon, 1959).
- [69] J. O. Hirschfelder, C. F. Curtiss, and R. B. Bird, *Molecular Theory of Gases and Liquids* (Wiley, New York, 1954).
- [70] G.A. Fernandez, J. Vrabec, and H. Hasse, *Fluid Phase Equilibria* **221** (2004) 157 (2004).
- [71] K. Meier, A. Laesecke, and S. Kabelac, *J. Chem. Phys.* **121**, 3671 (2004).
- [72] K. Meier, A. Laesecke, and S. Kabelac, *J. Chem. Phys.* **122**, 014513 (2005).